ACS NANO

www.acsnano.org

Open Access

This article is licensed under CC-BY-NC-ND 4.0

ARTICLE

Platelet-Derived Apoptotic Vesicles Promote Bone Regeneration via Golgi Phosphoprotein 2 (GOLPH2)-AKT Signaling Axis

Yuhe Jiang, Yuan Zhu, Yuzi Shao, Kunkun Yang, Lei Zhu, Yunsong Liu, Ping Zhang, Xiao Zhang,* and Yongsheng Zhou*

Cite This: *ACS Nano* 2023, 17, 25070−25090

Read Online

ACCESS | Metrics & More | Article Recommendations | Supporting Information

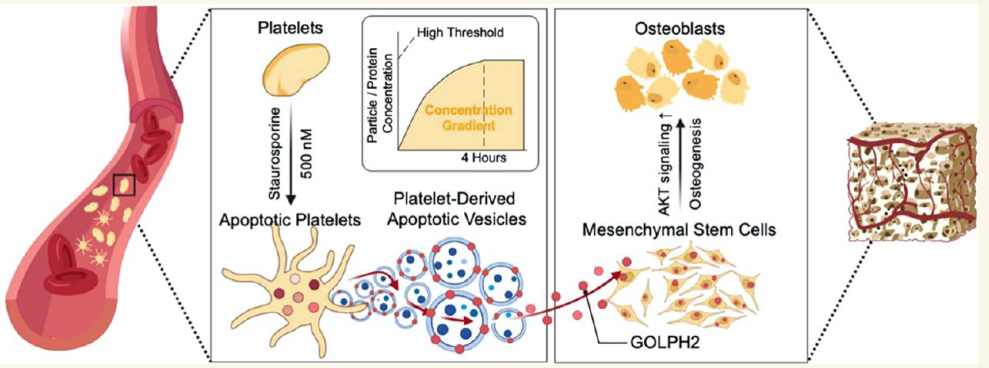

ABSTRACT: **Apoptotic vesicles (apoVs) are apoptotic-cell-derived nanosized vesicles that take on dominant roles in regulating bone homeostasis. We have demonstrated that mesenchymal stem cell (MSC)-derived apoVs are promising therapeutic agents for bone regeneration. However, clinical translation of MSC-derived apoVs has been hindered due to cell expansion and nuclear substance. As another appealing source for apoV therapy, blood cells could potentially eliminate these limitations. However, whether blood cells can release apoVs during apoptosis is uncertain, and the detailed characteristics and biological properties of respective apoVs are not elucidated. In this study, we showed that platelets (PLTs) could rapidly release abundant apoVs during apoptosis in a short time. To recognize the different protein expressions between PLT-derived apoVs and PLTs, we established their precise protein landscape. Furthermore, we identified six proteins specifically enriched in PLT-derived apoVs, which could be considered as specific biomarkers. More importantly, PLT-derived apoVs promoted osteogenesis of MSCs and rescued bone loss via Golgi phosphoprotein 2 (GOLPH2)-induced AKT phosphorylation, therefore, leading to the emergence of their potential in bone regeneration. In summary, we comprehensively determined characteristics of PLT-derived apoVs and confirmed their roles in bone metabolism through previously unrecognized GOPLH2-dependent AKT signaling, providing more understanding for exploring apoV-based therapy in bone tissue engineering.**

KEYWORDS: *apoptotic vesicles, platelets, mesenchymal stem cells, bone regeneration, Golgi phosphoprotein 2*

Apoptosis, a programmed cell death necessary for billions of cells to maintain homeostasis in the human body, comprises distinct chromatin condensation, cell shrinkage, and plasma blebbing.[1−3] Apoptotic vesicles (apoVs) are a heterogeneous nanosized extracellular vesicle (EV) population generated during this process, facilitating intercellular communication as a component of paracrine and participating in varied physiological and pathophysiological events. Recently, apoV-based therapies have been developed for various diseases, including inflammation,[4] cancer,[5] liver diseases,[6] diabetes,[7] atherosclerosis,[8] sepsis,[9] etc. Moreover, emerging evidence has revealed that apoVs could significantly promote tissue

Received: August 17, 2023
Revised: November 22, 2023
Accepted: November 28, 2023
Published: December 4, 2023

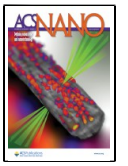

Downloaded via PEKING UNIV on December 28, 2023 at 07:27:14 (UTC).
See https://pubs.acs.org/sharingguidelines for options on how to legitimately share published articles.

ACS Publications

© 2023 The Authors. Published by American Chemical Society

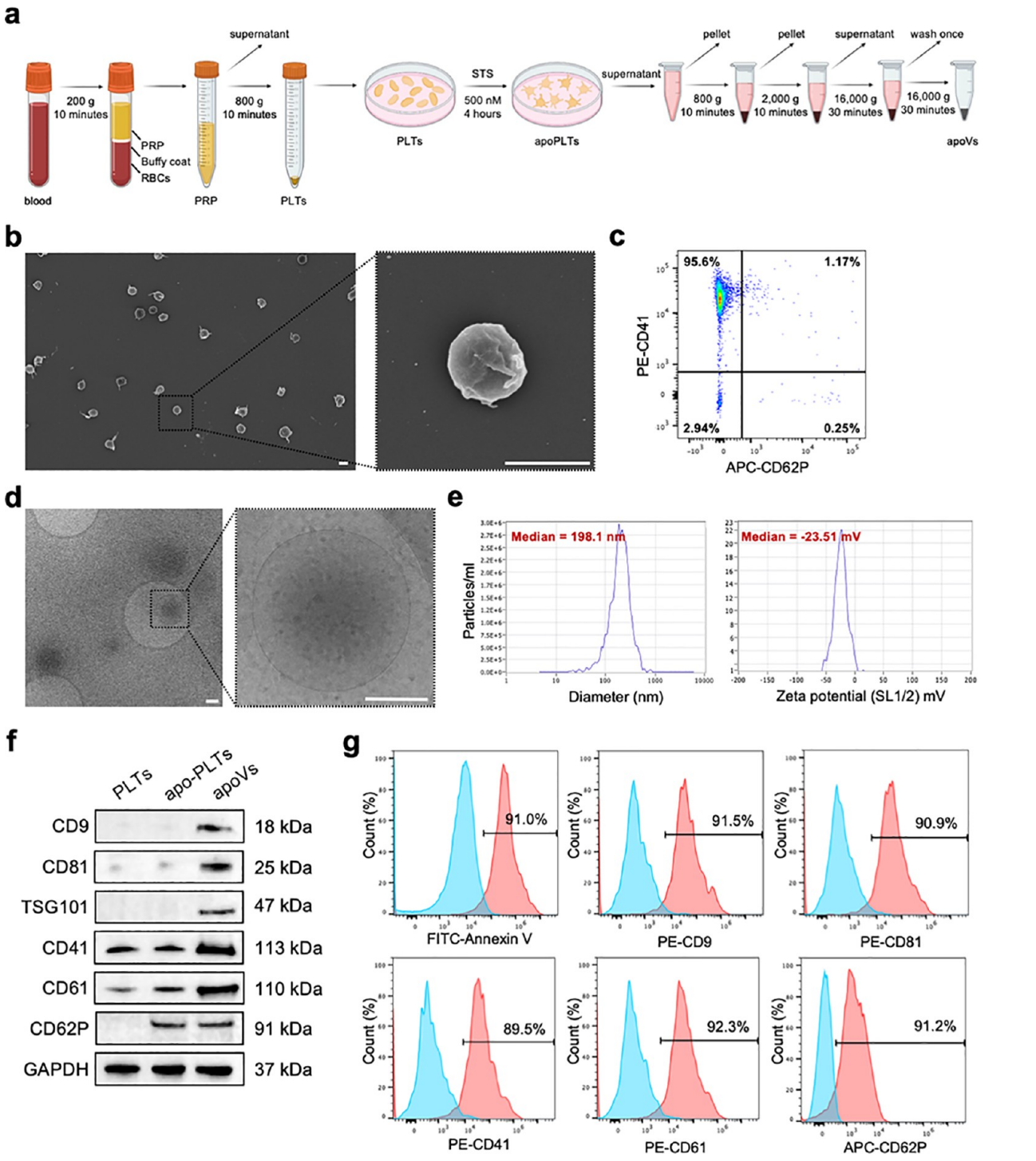

Figure 1. Characteristics of apoptotic vesicles (apoVs) derived from platelets (PLTs). (a) Schematic diagram indicating the procedures of isolating PLT-derived apoVs. (b) Representative scanning electron microscopic (SEM) images showing the morphology of PLTs. Scale bar: 2 μm. (c) Flow cytometric analysis identifying surface marker expression of PLTs. (d) Representative cryo-electron microscopy (Cryo-EM) images displaying the morphology of apoVs. Scale bar: 200 nm. (e) Nanoparticle tracking analysis by Zetaview exhibiting the size distribution (left panel) and membrane potential (right panel) of apoVs. (f) Western blotting analysis revealing enriched proteins of apoVs. (g) Flow cytometric analysis identifying surface markers expression of apoVs. The blue zone represents unstained apoVs (negative control); the red zone represents stained apoVs (experimental group). PRP, platelet-rich plasma; RBCs, red blood cells; STS, staurosporine; apoPLTs, apoptotic PLTs.

regeneration, such as bone,[10] muscle,[11] skin,[12] kidney,[13] etc. Our group has systemically elucidated detailed characteristics, specific biomarkers, and biological properties of apoVs derived from mesenchymal stem cells (MSCs).[14] Their functions in bone metabolism have been delineated as promoting osteogenesis and inhibiting osteoclast formation *in vitro* and *in vivo*.[15] However, cell culture and expansion are necessary to obtain enough vesicles, which lead to instabilities in both cell and EV function.[16,17] A possible immune issue eventuated by a nuclear substance is another concern.[18−20] Hence, a promising

https://doi.org/10.1021/acsnano.3c07717
ACS Nano 2023, 17, 25070−25090

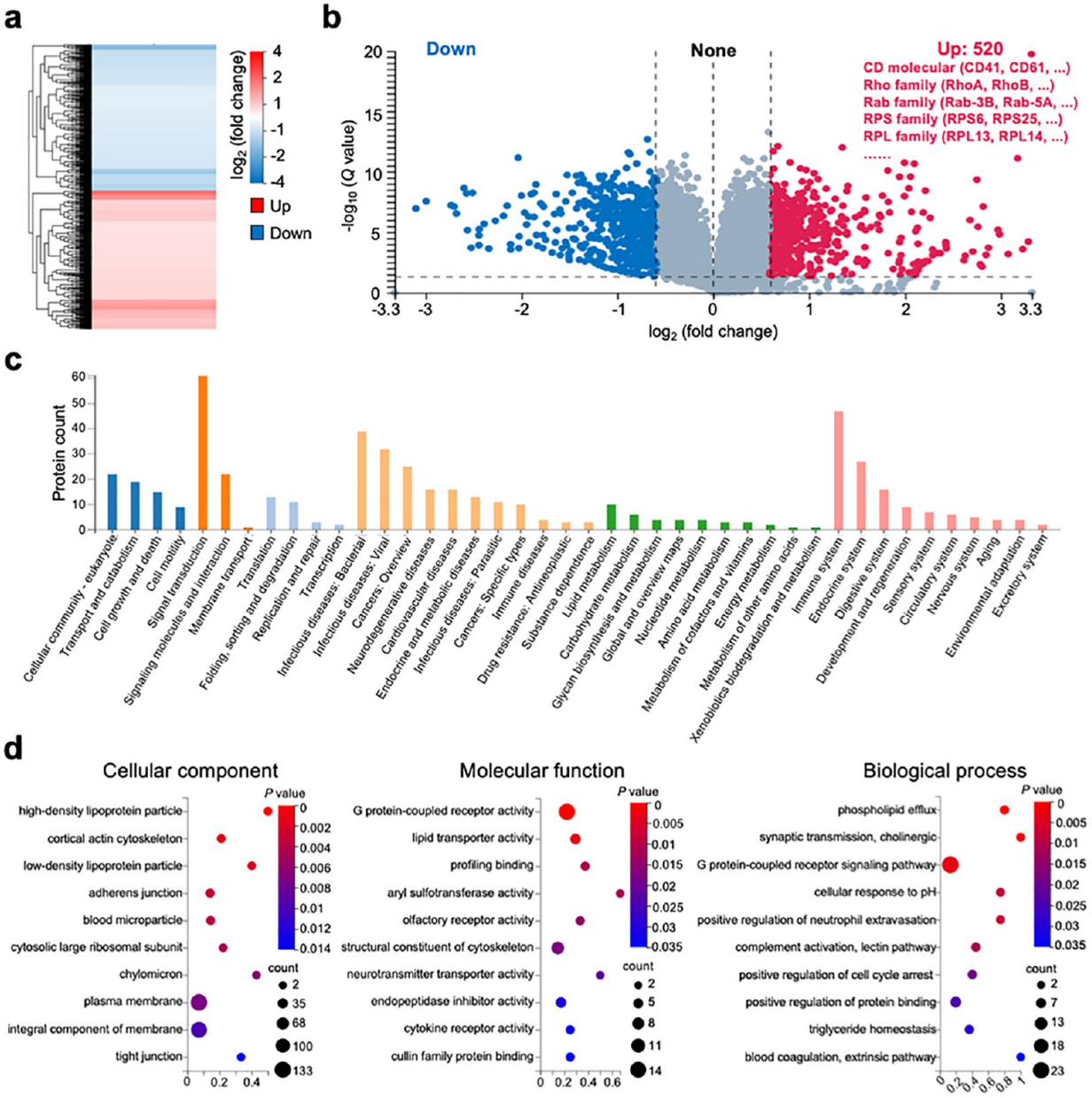

Figure 2. Proteomic mapping of PLT-derived apoVs. Fold change ≥ 2 and an adjusted *p* value < 0.05 were used to obtain differentially expressed proteins (DEPs). (a) Clustering heatmap of DEPs in apoVs compared to PLTs. The vertical axis represents proteins, and the horizontal axis represents the differential measure $\log_2$ (fold change). Enrichment is depicted in red and depletion in blue. (b) Volcano plots for upregulation (red dots) and downregulation (blue dots) of proteins in apoVs compared to PLTs. The total number of upregulated proteins is 520. (c) Kyoto Encyclopedia of Genes and Genomes (KEGG) pathway analysis of upregulated proteins in apoVs compared to PLTs. (d) Gene ontology (GO) enrichment analysis of upregulated proteins in apoVs compared to PLTs. The top 10 enriched terms of the three categories are presented as bubble charts. The vertical axis represents GO terms and the horizontal axis represents the enrichment ratio. The color of the bubble represents the enrichment significance, and the size of the bubble represents the number of proteins.

subpopulation of apoVs that need no cell amplification and without immunogenicity urgently needs to be identified.

Platelets (PLTs) are disc-shaped irregular components of blood.[21] Around 100 billion PLTs are produced by bone marrow residing megakaryocytes per day.[22] Compared to other cell sources, PLTs present irreplaceable advantages: (1) a large number of clinical allogenic PLTs can be obtained from whole-blood donation; (2) they are without nuclei and avoid cell expansion, diminishing issues on safety; (3) a lack of growth medium components reduces contamination concerns.[23] PLTs show active metabolism during their momentary life (close to 10 days in circulation).[24] Current studies concentrate on platelet-derived extracellular vesicles (PEVs), such as microvesicles and exosomes. PEVs have been shown to play important roles in coagulation,[25] immune regulation,[26] wound healing[27] and cancer development.[28] In addition, PEVs also possess regenerative effects in angiogenesis,[29,30] neurogenesis,[31,32] muscle regeneration,[33] etc. Nevertheless, expensive equipment and a complex extraction process impede popularization.[34] Therefore, a PEV population with a high yield and simple extraction method urgently needs to be developed.

The current research on PLT apoptosis focuses on the intrinsic apoptosis program and thrombocytopenic conditions.[22,35] The vesicles secreted during PLT apoptosis are

https://doi.org/10.1021/acsnano.3c07717
ACS Nano 2023, 17, 25070−25090

undefined. Their characteristics and biological significance remain unknown. Further, whether PLT-derived apoVs could break through barriers in apoV-therapy and PEV-application becomes the focal point of this paper.

RESULTS AND DISCUSSION

Isolation and Characterization of PLT-Derived ApoVs. Isolation of human PLTs was carried out as previously reported (Figure 1a).[36] The morphology and size distribution of PLTs were measured by scanning electron microscope (SEM). The size distribution ranged from 1.3 to 2.2 μm, and the average diameter was 1.75 μm, which was consistent with a previous report (Figure S1a,b).[37] In addition, these PLTs showed typical spherical morphology, which was in line with the characterization of unactivated PLTs (Figure 1b).[38] Therefore, these isolated PLTs exhibited good homogeneity. Moreover, these PLTs showed high expression of the PLT-specific marker (CD41) and low expression of the PLT-activation marker (CD62P), suggesting these cells met the universal standard of high-purity PLTs (Figure 1c).[39,40]

Staurosporine (STS) has been used to induce MSC apoptosis in our previous studies.[14,15] To explore optimal induction conditions, we stimulated PLTs with different concentrations of STS and tracked the continuous release of apoVs. These apoVs were separated from apoptotic PLTs (apoPLTs) using an optimized gradient centrifugation scheme (Figure 1a).[14] Results exhibited that STS of 500 nM or above could induce rapid release of apoVs within 4 h (Figure S2a,b). Regardless of STS concentration, the high threshold of released apoVs was almost identical and 6−8 times greater than physiological PEVs isolated from equivalent PLTs (Figure S2c). Specifically, the volume of blood we collected was 2 mL per individual. Around 2×10^8 PLTs could be isolated from a 2 mL blood sample, which could release 3.72×10^{11} apoVs (that is, one PLT could release 1860 apoVs) or 5.34×10^{10} PEVs (that is, one PLT could generate 267 PEVs) on average. Therefore, PLT-derived apoVs are promised to be mass-produced *in vitro* with STS induction (500 nM). The acquisition time was compressed within 6 h, laying the foundation for immediate application in the clinic.

Essential Properties of PLT-Derived ApoVs. PLT-derived apoVs were characterized in terms of morphology, size distribution, and biomarkers.[41] Their properties include a typical spherical-shaped morphology (Figure 1d), lipid bilayer membrane (Figure 1d), size distribution of 100−500 nm (Figure 1e), mean membrane potential of −29.84 mV (Figure 1e), surface exposure of phosphatidylserine (PS; Figure 1g), and abundance of general EV markers including an ESCRT component (TSG101) and tetraspanins (CD9 and CD81; Figure 1f,g).[42] In addition, PLT-derived apoVs inherited properties from parental cells and enriched surface signatures of PLTs and apoPLTs (CD41, CD61, and CD62P), distinguishing them from apoVs from other cell sources (Figure 1f,g). Herein, we revealed essential characteristics of PLT-derived apoVs, discovering they not only conformed to the universal properties of apoVs but also inherited biomarkers from parental cells.

Proteomic Profiling of PLT-Derived ApoVs. To characterize protein constituents precisely, we extracted proteins of PLTs and apoVs, and subsequently performed proteomic analysis as our anterior research.[14] Blood samples were collected from six different volunteers. In the aggregate, nearly 8200 proteins were certified (Table S1). Proteomic results showed 99.5% of proteins in apoVs and PLTs were in common. Despite considerable overlap, 520 proteins were upregulated, and 552 proteins were downregulated significantly in apoVs compared to PLTs (Figure 2a,b). The top 100 up-regulated and down-regulated proteins are listed in Tables S2 and S3, respectively. The functional analyses were instituted on the upregulated proteins in apoVs compared to PLTs. Kyoto Encyclopedia of Genes and Genomes (KEGG) pathway analysis manifested that these proteins were associated with the "cellular community" within the "cellular processes" domain; "signal transduction" within the "environmental information processing" domain; "translation" within the "genetic information processing" domain; "infectious diseases" within the "human diseases" domain; "lipid metabolism" within the "metabolism" domain; and "immune system" and "endocrine system" within the "organismal systems" domain (Figure 2c). Considering gene ontology (GO) enrichment, cellular component analysis indicated that a considerable proportion of proteins belonged to the "integral component of membrane" and "plasma membrane;" molecular function analysis showed that "G protein-coupled receptor activity" accounted for the largest proportion, followed by "lipid transporter activity"; biological process analysis revealed that the majority of proteins participated in the "positive regulation of protein binding" and "G protein-coupled receptor signaling pathway" (Figure 2d). These observations validated that PLT-derived apoVs enriched abundant proteins had to do with cellular metabolism, cellular transport, cellular behavior, and regulation of various diseases.

This is an interesting disclosed comparison of protein profile between PLTs and their apoptotic products, not only displaying the protein landscape of PLT-derived apoVs but also providing a worthy insight for PLT apoptosis. While PLTs and PEVs have attracted substantial attention, our understanding of PLT apoptosis is still very limited.[43−46] In this study, we have demonstrated several aspects about PLT apoptosis: (1) Under induction of STS, PLTs undergo apoptosis in a much shorter time than nucleated cells (such as MSCs). (2) PLTs release a large amount of apoVs during apoptosis, and the yield is much higher than traditional PEVs. (3) PLT-derived apoVs enrich plentiful functional proteins, which are different from PLTs and closely related to various cellular behaviors except for apoptosis. All of these aspects will inspire us to ponder deeply on the PLT apoptosis and PLT-derived apoVs and also provide more information for other researchers.

Specific Biomarkers of PLT-Derived ApoVs. On the basis of minimal information for studies of extracellular vesicles (MISEV) 2018 guidelines, those enriched proteins in EVs are classified into four categories.[41] In addition, to validate apoV identity, multiple vital apoptotic proteins have been regarded as apoptotic biomarkers.[47] According to protein quantification, atypical chemokine receptors (ACKR family) and CD molecules were assessed in category 1, belonging to transmembrane or glycosylphosphatidylinositol (GPI)-anchored proteins associated with the plasma membrane and/or endosomes; the most significant fold change was up to 7.84. The Rho family and Rab family were assessed in category 2, belonging to cytosolic proteins recovered in EVs; the most significant fold change was up to 3.68. A range of ribosomal proteins was assessed in category 3, belonging to ribosomal proteins; the most significant fold change was up to 3.71. Seizure-6-like protein (SEZ6L family) and Golgi phosphoproteins (GOLPH family) were assessed in category 4, belonging to transmembrane, lipid-bound, and soluble proteins associated with intracellular compartments other than PM/endosomes; the most significant

https://doi.org/10.1021/acsnano.3c07717
ACS Nano 2023, 17, 25070−25090

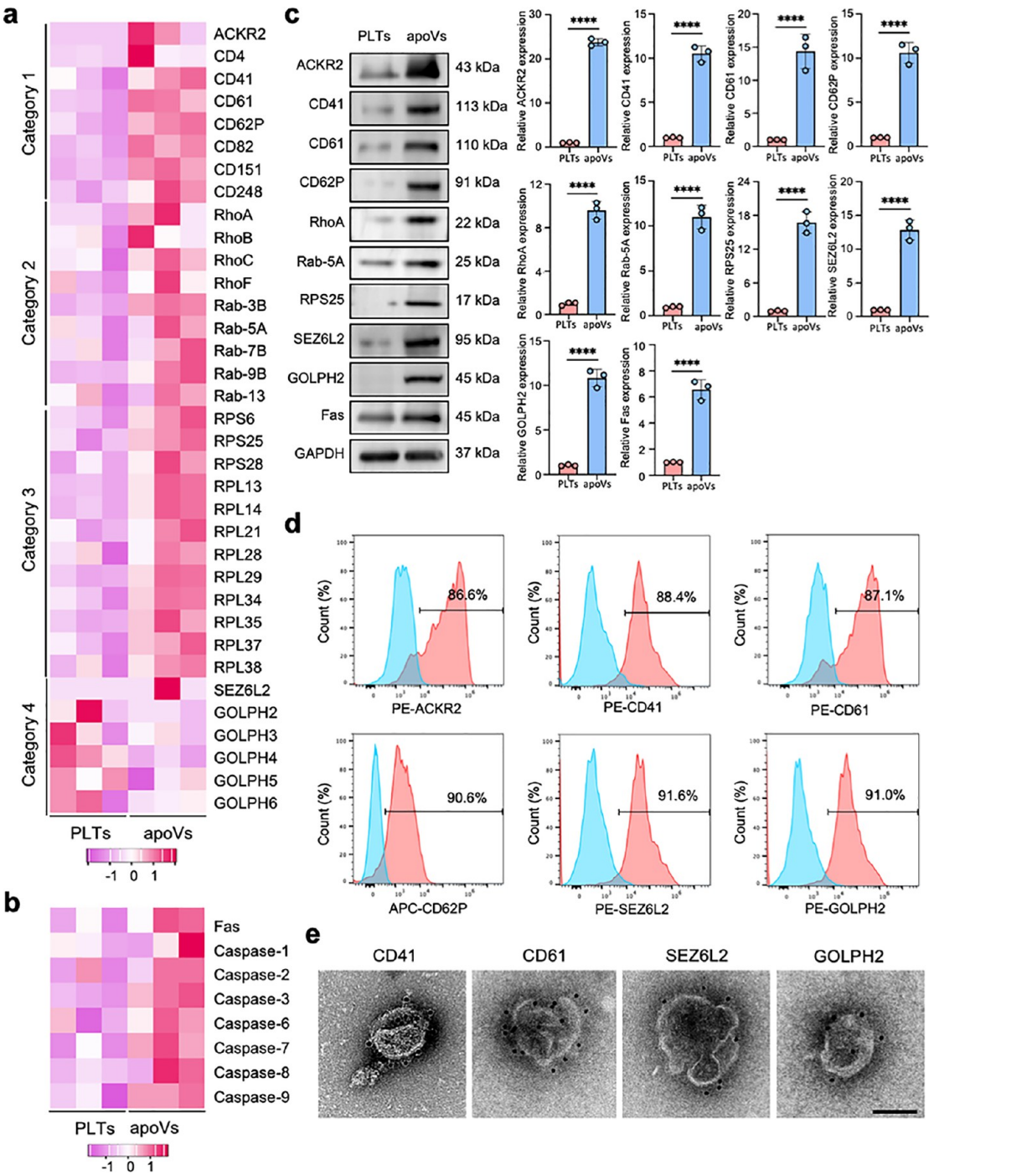

Figure 3. Specific biomarkers of PLT-derived apoVs. (a, b) Heatmaps exhibiting the DEPs of the four categories (a) and apoptotic markers (b) in apoVs compared to PLTs. Category 1: Transmembrane or glycosylphosphatidylinositol (GPI)-anchored proteins associated with plasma membrane and/or endosomes. Category 2: Cytosolic proteins recovered in EVs. Category 3: Ribosomal proteins. Category 4: Transmembrane, lipid-bound, and soluble proteins associated with other intracellular compartments than PM/endosomes. Rows represent proteins, and columns represent individual replicates. Fold change of proteins in apoVs versus PLTs is color-coded, of which red represents up-regulation and purple represents down-regulation. The darker the color, the higher the extent. (c) Western blotting and densitometric analysis showing the enriched proteins of PLT-derived apoVs. (d) Flow cytometric analysis identifying specific markers in apoVs. The blue zone represents unstained apoVs (negative control); the red zone represents stained apoVs (experimental group). (e) Immuno-electron microscopy analysis of CD41, CD61, SEZ6L2, and GOLPH2 in apoVs. The black dots are gold particles, which localized at the apoV periphery. Scale bar: 100 nm. Data are presented as mean ± standard deviation (SD). Statistical analyses are performed by one-way ANOVA with the Tukey's post hoc test for multiple group comparisons. ****$p < 0.0001$. SEZ6L2, seizure 6-like protein 2; ACKR2, atypical chemokine receptor 2; GOLPH2, Golgi phosphoprotein 2.

fold change was up to 8.43. The Fas and Caspase families were identified as apoptotic biomarkers; the most significant fold change was up to 2.17 (Figure 3a,b). These proteins represented the core proteome of PLT-derived apoVs.

https://doi.org/10.1021/acsnano.3c07717
ACS Nano 2023, 17, 25070−25090

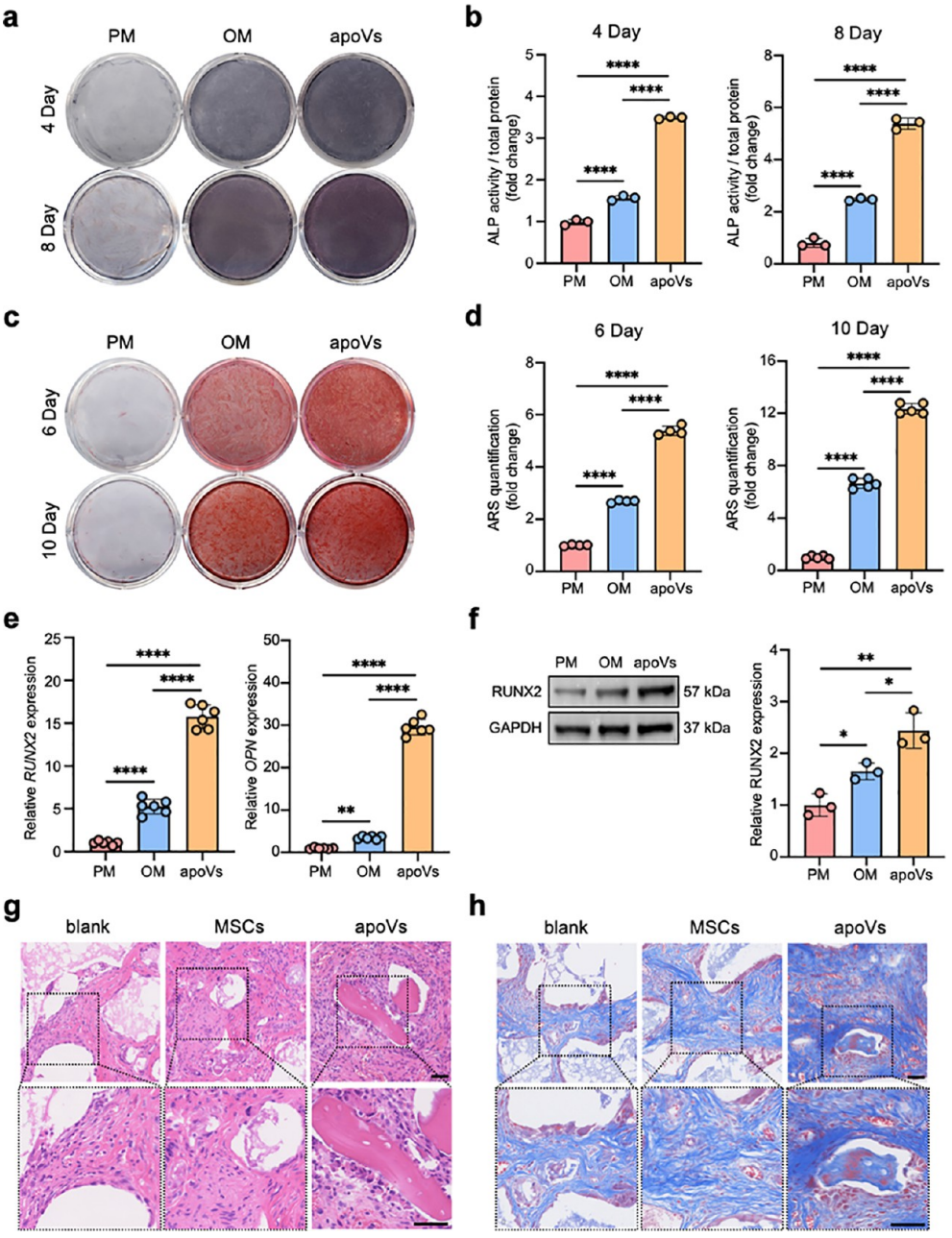

Figure 4. PLT-derived apoVs promote the osteogenesis of MSCs. MSCs were cultured in proliferation medium (PM group), osteogenic induction medium (OM group), or OM with 100 ng/mL apoVs (apoV group) for 4−10 days. (a,b) Alkaline phosphatase (ALP) staining and quantification detecting ALP activities. (c,d) Alizarin red S (ARS) staining and quantification of mineralized absorbance assessing mineralization. (e) Real-time quantitative polymerase chain reaction (RT-qPCR) examining the expression of osteogenic genes. (f) Western blotting and densitometric analysis exhibiting the expression of the osteogenic marker. Nude mice were randomly separated into three groups (N = 4) and implanted with β-TCP particles (blank group), β-TCP-particle-loaded MSCs (MSC group), β-TCP-particle-loaded MSCs pretreated with apoVs (apoV group). (g) Hematoxylin and eosin (H&E) staining of implants. The bone matrix is stained pink. Scale bar: 50 μm. (h) Masson's trichrome staining of implants. The collagen and ostein are stained blue-green. Scale bar: 50 μm. Data are presented as mean ± standard deviation (SD). Statistical analyses are performed by one-way ANOVA with Tukey's post hoc test for multiple group comparisons. *p < 0.05, **p < 0.01, ****p < 0.0001.

At present, specific markers that could identify PLT-derived apoVs are lacking. To discover apoV markers, we used Western blotting combined with proteomic analysis for accurate protein quantification. Since we have determined the core proteome of PLT-derived apoVs (Figure 3a,b), we further confirmed the presence of 10 of candidate proteins in PLT-derived apoVs by Western blotting. The rationale for selecting these 10 biomarkers was based on (1) ubiquitous markers of apoVs which were determined in our previous studies,[14] including RhoA, Rab-5A, RPS25, and Fas; (2) specific biomarkers of parental cells,[40] including CD41, CD61, and CD62P; (3) significant higher expression in apoVs compared to PLTs, including ACKR2, SEZ6L2, and GOLPH2. Western blotting results showed that 10 candidate proteins were enriched in apoVs, and the corresponding quantitative analysis further indicated that these 10 candidate proteins were significantly

https://doi.org/10.1021/acsnano.3c07717
ACS Nano 2023, 17, 25070−25090

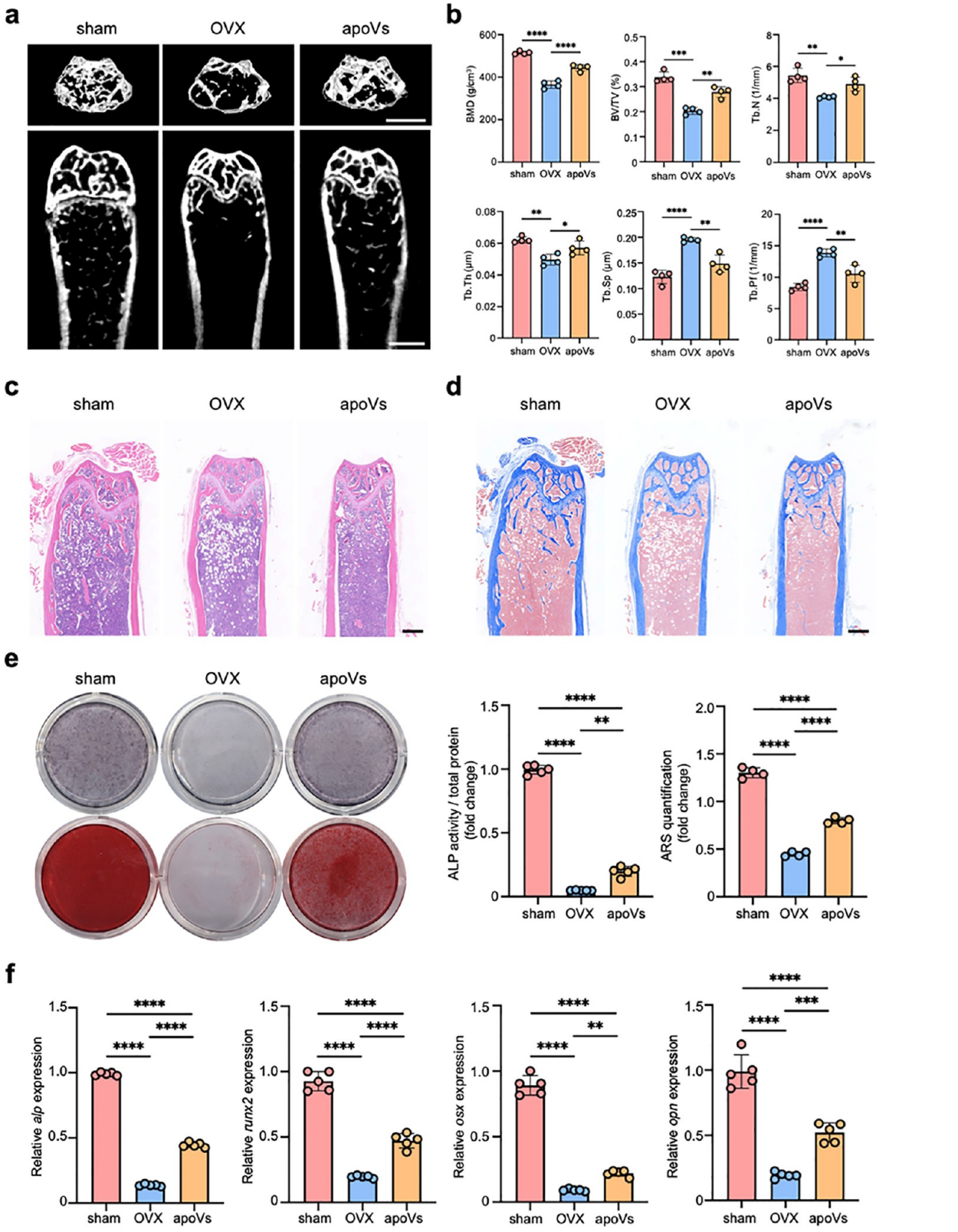

Figure 5. PLT-derived apoVs attenuate bone loss induced by estrogen deficiency in ovariectomized (OVX) mice. (a) 3D reconstruction images and longitudinal section images of trabecular bone in distal femurs. Scale bar: 1 mm. (b) Bone histomorphometry of distal femurs. (c) H&E staining of distal femurs. Scale bar: 500 μm. (d) Masson's trichrome staining of distal femurs. Scale bar: 500 μm. (e) ALP staining/quantification and ARS staining/quantification assessing *in vitro* osteogenic differentiation ability of mice MSCs (mMSCs). (f) RT-qPCR examining osteogenic gene expressions in mMSCs. Data are presented as mean ± standard deviation (SD). Statistical analyses are performed by one-way ANOVA with Tukey's post hoc test or Welch's ANOVA with Dunnett's T3 post hoc test for multiple group comparisons. *$p < 0.05$, **$p < 0.01$, ***$p < 0.001$, ****$p < 0.0001$. BMD, bone mineral density; BV/TV, bone volume/total bone volume; Tb.N, trabecular number; Tb.Th, trabecular thickness; Tb.Sp, trabecular spacing; Tb.Pf, trabecular bone pattern factor.

https://doi.org/10.1021/acsnano.3c07717
ACS Nano 2023, 17, 25070−25090

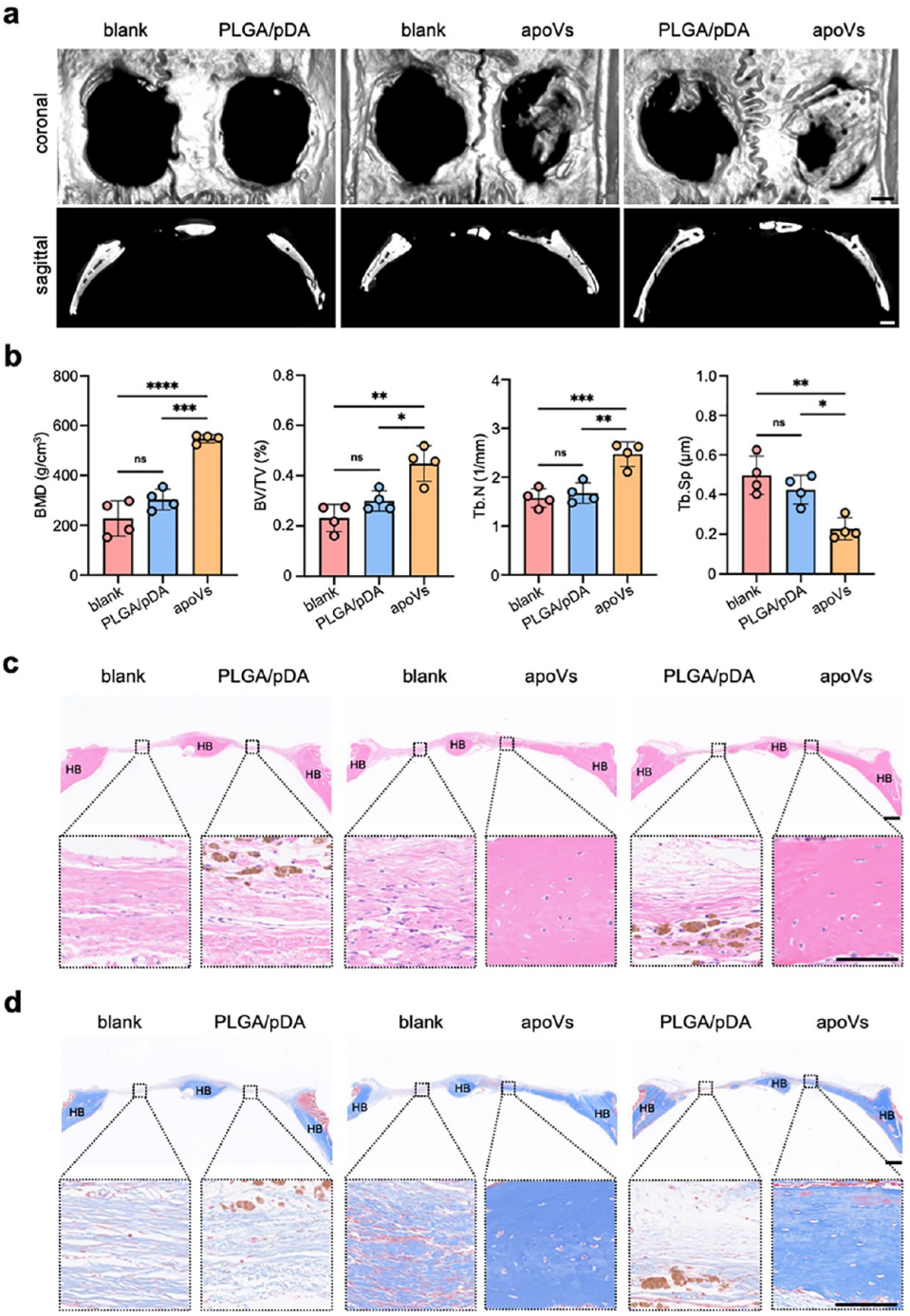

Figure 6. PLT-derived apoVs increase bone formation in rat calvarial defects. (a) Micro-CT images representing cross and sagittal sections of defect areas. Scale bar: 1 mm. (b) Bone histomorphometry of defect areas. (c) H&E staining characterizing the neo-generated tissues. Scale bar: 1 mm (upper images), 100 μm (lower images). (d) Masson's trichrome staining of the neo-generated tissues. Scale bar: 1 mm (upper images), 100 μm (lower images). Data are presented as mean ± standard deviation (SD). Statistical analyses are performed by one-way ANOVA with a Tukey's post hoc test for multiple group comparisons. ns, no significant; *$p < 0.05$, **$p < 0.01$, ***$p < 0.001$, ****$p < 0.0001$. BMD, bone mineral density; BV/TV, bone volume/total bone volume; Tb.N, trabecular number; Tb.Sp, trabecular spacing; HB, host bone.

upregulated in apoVs compared with PLTs (the fold change ranged from 6.56 to 23.79, Figure 3c). The enrichment of RhoA, Rab-5A, RPS25, and Fas in PLT-derived apoVs supported these proteins as general apoV markers and expanded the sphere of application for the apoV biomarker candidate pool.[14] In addition, we performed flow cytometric analysis to further confirm the enrichment of six specific markers (CD41, CD61, CD62P, ACKR2, SEZ6L2, and GOLPH2) in PLT-derived apoVs. The results were in line with proteomic and Western blotting analysis, which determined the accumulation of these six specific proteins in apoVs (Figure 3d). Moreover, observations on the colocalization of gold nanoparticles (NPs) and target proteins intuitively verified the presence of CD41, CD61, SEZ6L2, and GOLPH2 on the apoV membrane (Figure 3e). The number of gold NPs illustrated high expression of these proteins.[48] Collectively, these results verified six specific proteins

https://doi.org/10.1021/acsnano.3c07717
ACS Nano 2023, 17, 25070−25090

in PLT-derived apoVs, representing a series of specific biomarkers.

PLT-Derived ApoVs Promote MSC Osteogenesis *in Vitro* and *in Vivo*. PLT-derived apoVs below or equal to 200 ng/mL were not toxic to human MSCs (Figure S3). The incorporation of apoVs was shown by a gradual increase of red dots (PKH26-labeled apoVs) in MSCs between 3 and 48 h, followed by a decrease, which might be a result of cell metabolism (Figure S4). Then, MSCs were incubated in osteogenic medium (OM) with a gradient ascending concentration of apoVs, of which 100 ng/mL of apoVs had a pronounced osteoinductive effect (Figure S5a,b). The increased osteogenic differentiation stimulated by apoVs *in vitro* was further displayed by ALP staining/quantification (Figure 4a,b) and alizarin red S (ARS) staining/quantification (Figure 4c,d). The upregulation of osteogenic genes and proteins was detected through real-time quantitative polymerase chain reaction (RT-qPCR; Figure 4e) and Western blotting (Figure 4f). To clarify osteoinductivity *in vivo*, MSCs were cultured without or with apoVs in a proliferation medium (PM) for 5 days. Then, MSCs were loaded in beta-tricalcium phosphate (β-TCP) scaffolds and heterotopically transplanted in nude mice. Histological staining showed that β-TCP-scaffold-loaded MSCs were full of compact fibrous tissues, while scaffold-loaded apoV-treated MSCs brought about ectopic bone-like tissue characterized by a homogeneous bone matrix with a few cells and lacunae (Figure 4g,h).

Taken together, apoVs facilitate osteogenic differentiation of MSCs *in vitro* and *in vivo*, filling the gap in PLT-derived apoV functional research. It is noticed that the active concentration of PLT-derived apoVs is half that of the MSC-derived apoVs;[15] directing a small amount of blood could meet treatment needs. Less dosage is also convenient for material loading, broadening the application scenarios of PLT-derived apoVs. In addition, compared with the OM group, ALP and ARS staining exhibited significant differences in the early stage of osteogenic induction, directing PLT-apoVs to possess superior osteoinductivity.

PLT-Derived ApoVs Alleviate Bone Loss under Estrogen Deficiency-Induced Osteoporosis. We investigated the therapeutic efficacy of apoVs in restoring bone homeostasis in ovariectomized (OVX) mice. Biodistribution of EVs is particularly important to determining their targeting level.[49] At 12, 24, and 48 h after tail vein injection, fluorescence imaging showed those DiR-labeled apoVs mostly enriched in the liver, implying hepatic metabolism (Figure S6a,b). Over time, apoV enrichment in the femur gradually increased, suggesting that the PLT-derived apoVs reached the femur and performed their function within a period (Figure S6a,b).

OVX mice were randomly separated into two groups and injected with apoVs (apoV group) or vehicle (OVX group) via the tail vein once a week. After 8 weeks, venous blood routine and visceral histological staining exhibited no significant difference among groups, confirming the biosafety of apoVs (Figure S7a,b). Microcomputed tomography (micro-CT) and 3D reconstruction (Figure 5a), analysis of bone mineral density (BMD) and bone microarchitectural indices (Figure 5b), and histological examination (Figure 5c,d) of distal femurs showed estrogen deficiency-induced significant bone loss in mice, while prominent improvement of bone mass was exhibited after apoV treatment. These observations exhibited that apoVs alleviated bone loss effectively under estrogen-deficiency-induced osteoporosis. Endogenous mice MSCs (mMSCs) were extracted and cultured in OM. As indicated by ALP activity, mineralization, and osteogenic gene expression, OVX mMSCs possessed an attenuated osteogenic capacity compared to sham mMSCs, while apoV treatment could significantly rescue their osteogenic properties (Figure 5e,f). Altogether, the systematic delivery of apoVs rescued stem cell properties and therefore regulated bone remodeling in osteoporosis, offering important knowledge for the development of apoV therapy.

ApoVs, as nanoparticles derived from apoptotic cells, are considered to have biocompatibility and reduced immunogenicity compared with other synthetic nanoparticles.[50,51] However, due to the unwanted off-target activities and potential "dilution effects" during systemic administration, which may affect their ability to reach the target tissue, the use of apoVs in therapeutic applications may be limited.[52,53] Increasing evidence have shown that EVs could be engineered or modified to improve their efficiency, specificity, and safety in treatment.[54−56] Likewise, to fully exploit the apoV therapeutic potential in bone regeneration, engineering treatment should be considered.

PLT-Derived ApoVs Promote Bone Healing in Critical-Sized Calvarial Defects. According to our previous research, dopamine-coated poly lactic-*co*-glycolic acid (PLGA/pDA) scaffolds displayed a sustained-release effect after loading exosomes.[57] Therefore, we performed apoV immobilization, as described. PKH26-labeled apoVs (red dots) were uniformly distributed on the surface of PLGA/pDA substrates, with PKH26-stained PLGA/pDA substrates as a control (Figure S8a). *In vitro*, vesicle release kinetics in saline showed a slow and controlled profile of apoVs from the PLGA/pDA substrates during a 14-day monitoring span (Figure S8b).

PLGA/pDA scaffolds (PLGA/pDA group) or PLGA/pDA scaffold-loaded apoVs (apoV group) were implanted into critical-size calvarial defects created in adult rats for 8 weeks. Venous blood routine and visceral histological staining verified apoV biosafety (Figure S9a,b). Micro-CT images displayed that the defects in the blank control and PLGA/pDA group were almost lacking healing, while high-density spots and peninsulas of bone nodule formation along the margins of bone defects were discovered in the apoV group (Figure 6a). Bone histomorphometry analysis revealed no significant difference between the blank control and PLGA/pDA group, while bone healing appeared after apoV transplantation (Figure 6b). Moreover, histological staining showed that the defects in the blank control or treated with PLGA/pDA scaffolds were filled with fibrotic connective tissues, while defects transplanted to apoVs resulted in lamellar bone formation nearly bridging the defect area (Figure 6c-d).

Taken overall, PLT-derived apoVs from 1 mL of human whole blood is sufficient to heal a xenogeneic defect of 5 mm diameter, implying the localized transplantation of apoVs could induce robust bone formation in nonhealing *in situ* defects. Cell-free tissue-engineered bone constructed with PLT-derived apoVs as the core is an attractive therapeutic modality for bone regeneration. More importantly, apoVs derived from rat autologous PLTs exhibited outstanding osteoinduction in bone defects, indicating the possibility of self-use (Figure S10a−d). Autologous PLTs avoid immunological rejection and ethical apprehension and avert *in vitro* cell culture and expansion, offering a promising approach to cell-free bone tissue engineering.

PLT-Derived ApoVs Regulate MSC Osteogenesis via GOLPH2 and AKT Phosphorylation. To reveal the mechanism underlying apoV-mediated MSC osteogenesis, we performed a proteomic analysis. MSCs were isolated from four

https://doi.org/10.1021/acsnano.3c07717
ACS Nano 2023, 17, 25070−25090

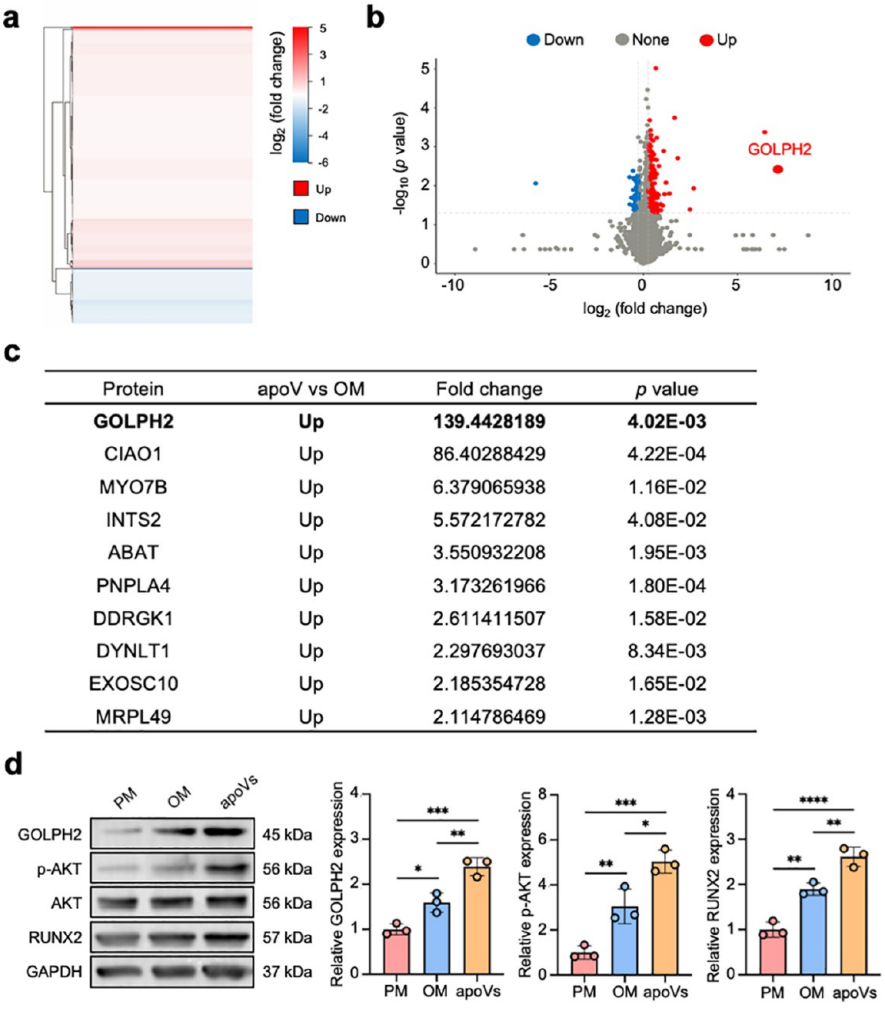

c

Protein	apoV vs OM	Fold change	*p* value
GOLPH2	**Up**	**139.4428189**	**4.02E-03**
CIAO1	Up	86.40288429	4.22E-04
MYO7B	Up	6.379065938	1.16E-02
INTS2	Up	5.572172782	4.08E-02
ABAT	Up	3.550932208	1.95E-03
PNPLA4	Up	3.173261966	1.80E-04
DDRGK1	Up	2.611411507	1.58E-02
DYNLT1	Up	2.297693037	8.34E-03
EXOSC10	Up	2.185354728	1.65E-02
MRPL49	Up	2.114786469	1.28E-03

Figure 7. Comparison of proteomic profile between MSCs with or without apoV induction. MSCs were cultured in OM (OM group) or OM with 100 ng/mL apoVs (apoV group). Fold change ≥ 2 and an adjusted *p* value < 0.05 were used to obtain DEPs. (a) Clustering heatmap of DEPs in apoV group compared to the OM group. The vertical axis represents proteins, and the horizontal axis represents the differential measure log 2 (fold change). Enrichment is depicted in red and depletion in blue. (b) Volcano plots for upregulation (red dots) and downregulation (blue dots) of proteins in the apoV group compared to the OM group. (c) Top 10 upregulated proteins in the apoV group compared to the OM group. (d) Expression of pivotal proteins (GOLPH2, AKT, p-AKT, and RUNX2) in MSCs. Data are presented as mean ± standard deviation (SD). Statistical analyses are performed by one-way ANOVA with Tukey's post hoc test for multiple group comparisons. *$p < 0.05$, **$p < 0.01$, ***$p < 0.001$, ****$p < 0.0001$.

different donors. In the mass, around 5700 proteins were certificated (Table S4). A total of 246 proteins were upregulated, and 56 proteins were downregulated in the apoV group compared to the OM group (Figure 7a,b). Eukaryotic ortholog groups (KOG) manifested that the differentially expressed proteins (DEPs) were predominantly associated with "signal transduction mechanisms" and "post-translational modification, protein turnover" (Figure S11a). Functional annotations, including KEGG pathway analysis (Figure S11b) and GO enrichment analysis (Figure S12), verified that MSCs after apoV induction were enriched with proteins predominantly related to protein binding and signal transduction.

Quantitative protein spectroscopy enumerated the top 10 upregulated proteins in MSCs after apoV induction (Figure 7c). From these proteins, we noticed GOLPH2 because of prominent expression change (fold change = 139.4), which was way above other proteins. It is also a candidate specific biomarker enriched in apoVs as shown before. Notably, Western blotting verified GOLPH2 upregulated in the apoV group, proving the reliability of the protein profile (Figure 7d). GOLPH2 is intimately related to the Golgi apparatus, which is the central component of the mammalian secretory pathway.[58] It has been reported to be indispensable to the endochondral bone formation during early development as an interacting partner with osteogenic key proteins through Golgi-related trafficking.[59] However, the specific mechanism of GOLPH2 in MSC osteogenic differentiation is uncovered.

Western blotting showed similar upward trends of GOLPH2 and RUNX2 in MSCs after apoV induction (Figure 7d). Considering that GOLPH2 was specifically enriched in apoVs and verified significantly in MSCs after apoV induction, we hypothesized that GOLPH2 might modulate MSC osteogenesis. To clarify its role, we performed lentiviral short-hairpin RNA (shRNA) interference. GOLPH2 was stably knocked down in MSCs (Figure S13a). Less intensive ALP activity (Figure S13b,c), diminished deposition of minerals (Figure S13d,e), and downregulation of osteogenesis-related genes (Figure S13f) and proteins (Figure S13g) were observed in

https://doi.org/10.1021/acsnano.3c07717
ACS Nano 2023, 17, 25070−25090

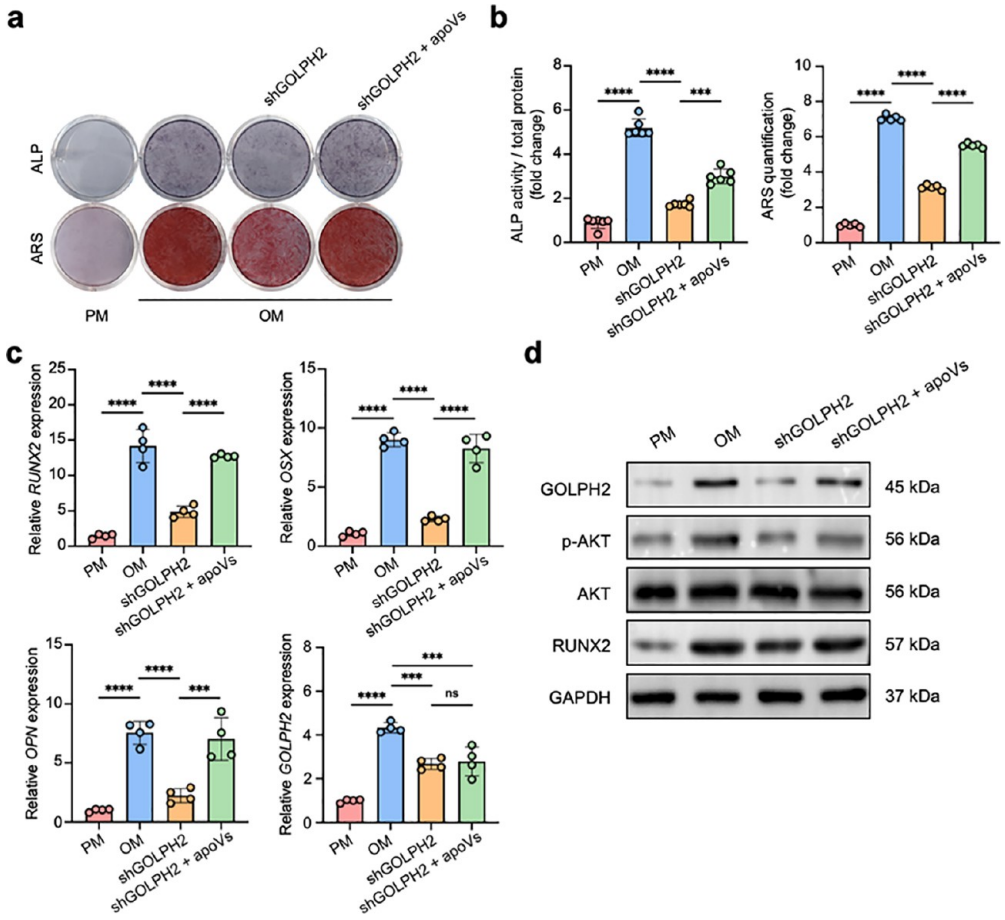

Figure 8. PLT-derived apoVs rescue MSC osteogenesis downregulation via recovering GOLPH2. ShGOLPH2 knocked-down MSCs were cultured in OM (shGOLPH2 group) or OM with 100 ng/mL apoVs (shGOLPH2 + apoV group) for 4−10 days. ApoVs rescue shGOLPH2-MSC osteogenesis as indicated by ALP staining/quantification (a, b), ARS staining/quantification (a, b), RT-qPCR analysis (c), and Western blotting (d). Data are presented as mean ± standard deviation (SD). Statistical analyses are performed by one-way ANOVA with Tukey's post hoc test or Welch's ANOVA with Dunnett's T3 post hoc test for multiple group comparisons. ns, no significant, ***$p < 0.001$, ****$p < 0.0001$.

shGOLPH2MSCs compared to a negative control (NC group), supporting GOLPH2 as an up-regulator in MSC osteogenesis. Furthermore, multiple evidence has considered GOLPH2 as an activator of the AKT signaling pathway,[60,61] which implicates cell differentiation and bone remodeling.[62,63] The upregulation of GOLPH2 in MSCs accompanied by a p-AKT increase also supported us in speculating that apoV-mediated MSC osteogenesis is relevant to GOLPH2 and phosphorylation of AKT (Figure 7d).

After GOLPH2 knockdown, apoVs were applied to the shGOLPH2MSCs. Consistent with previous reports, GOLPH2 deficiency led to AKT phosphorylation downregulation while GOLPH2 recovery led to AKT phosphorylation upregulation, indicating GOLPH2 as an up-regulator of AKT signaling (Figure 8d). It was also observed that the decrease of shGOLPH2MSC osteogenesis along with GOLPH2 and p-AKT upturned after apoV induction, proving apoVs rescued MSC osteogenesis downregulation via recovering GOLPH2 protein level and activating AKT signaling (Figure 8a−d). Moreover, the expression of the *GOLPH2* gene was stable in shGOLPH2MSCs with or without apoV treatment, suggesting that MSCs might be reused by GOLPH2 protein from apoVs (Figure 8c).

GOLPH2 is a Golgi resident protein, which has been considered to play a key role in maintaining cell proliferation and function.[64,65] Cumulative survival of mice with a severe truncation of the GOLPH2 C-terminus (GOLPH2(tr/tr)) was significantly reduced.[66] Thus, the *GOLPH2*-deleted model animal is unavailable. Meanwhile, PLTs do not have the ability of self-replication and cannot be cultured *in vitro*,[67] which means changing GOLPH2 expression in PLTs or apoVs via genome editing is not feasible.

According to proteomic profiling, protein cargo similarity between PLTs and apoVs was up to 99.5%, while the expression level of GOLPH2 in apoVs was significantly higher than that in PLTs (Figure 3c). Thus, PLTs were recognized as a control group in subsequent experiments. MSCs were cocultured with equivalent PLTs or apoVs in the presence of OM. ALP stain/quantification (Figure 9a,b), ARS stain/quantification (Figure 9a,b), RT-qPCR analysis of osteogenic genes (Figure 9c), and Western blotting of osteogenic proteins (Figure 9d) revealed that MSC osteogenesis did not change significantly with PLT incubation but increased with apoV treatment *in vitro*. Histological staining of heterotopic implants exhibited similar outcomes (Figure S15a,b). Thus, PLT-derived apoVs inherited and reinforced the osteoinductive properties of PLTs. In addition, the expression of GOLPH2 and p-AKT varied along with the change of RUNX2, indicating apoV-mediate MSC osteogenesis might relate to GOLPH2 and AKT phosphorylation (Figure 9d).

https://doi.org/10.1021/acsnano.3c07717
ACS Nano 2023, 17, 25070−25090

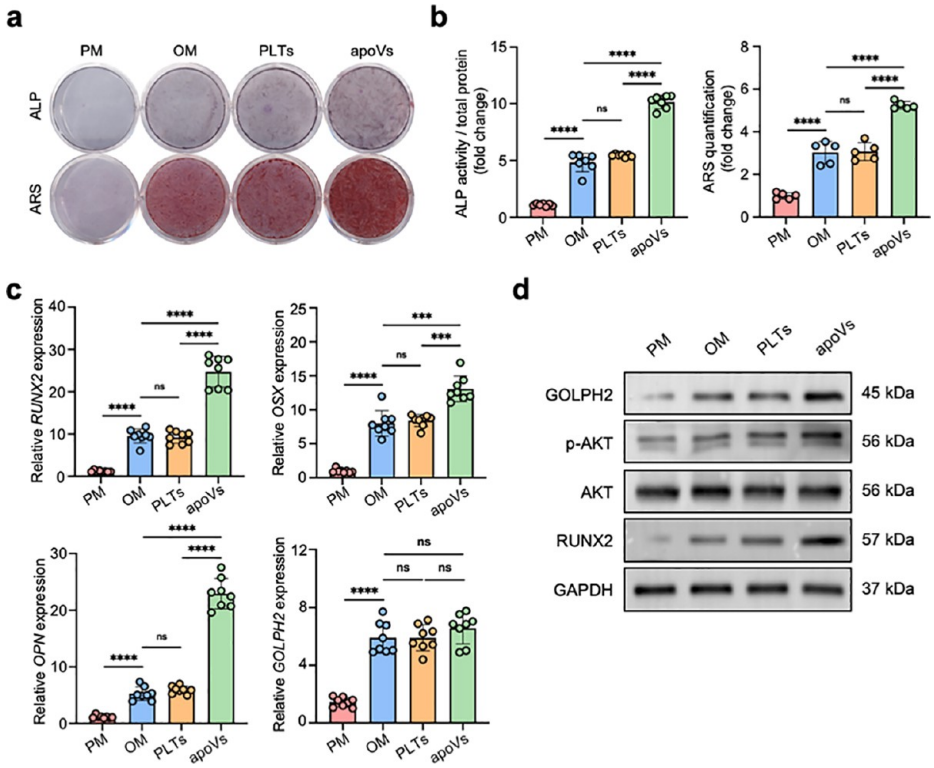

Figure 9. Osteoinductive capacity of apoVs is superior to equivalent PLTs. MSCs were cultured in PM (PM group), OM (OM group), OM with 100 ng/mL PLTs (PLT group), or apoVs (apoV group) for 4−10 days. (a,b) ALP activities in MSCs and mineralization of MSCs. (c) Expression of osteogenic genes and GOLPH2. (d) Expression of pivotal proteins. Data are presented as mean ± standard deviation (SD). Statistical analyses are performed by one-way ANOVA with Tukey's post hoc test or Welch's ANOVA with Dunnett's T3 post hoc test for multiple group comparisons. ns, no significant, ***$p < 0.001$, ****$p < 0.0001$.

Performing magnetic activated sorting as in our previous study,[14] we isolated a GOLPH2-negative apoV subpopulation (Figure S14a) and attested that GOLPH2 expression on the apoV membrane was reduced (Figure S14b). The influence of GOLPH2 deprivation in apoVs was represented as decreased osteoinductivity *in vitro* (Figure 10a−d) and *in vivo* (Figure S15a,b), proving that GOLPH2 might be responsible for apoV-mediated MSC osteogenesis. Notably, GOLPH2 protein levels in MSCs increased after apoV stimulation and decreased with GOLPH2 depletion (Figure 10d), while *GOLPH2* gene expression did not change significantly (Figure 10c), implying that recipient cells might utilize target protein from apoVs. Immunofluorescence staining further observed the uptake of GOLPH2 protein from apoVs to recipient MSCs within 24 h (Figure 10e). Moreover, synchronous variations of AKT phosphorylation and GOLPH2 suggested an intimate relationship between them (Figure 10d).

ApoV-Mediated Osteoinduction Depends on GOLPH2-Induced AKT Phosphorylation. MK-2206 is a selective allosteric inhibitor of AKT signaling, which has been applied in phase I and II clinical trials.[68,69] Here, the phosphorylation of AKT stimulated by apoVs was effectively intercepted with MK-2206 (Figure 11d). Downregulation of ALP activity (Figure 11a,b), mineralized nodule formation (Figure 11a,b), osteogenic gene expression (Figure 11c), osteogenic protein expression (Figure 11d), and ectopic bone-like tissue formation (Figure S15a,b) implied the osteoinduction of apoV was almost eliminated by MK-2206, proving apoVs enhanced MSC osteogenesis via activating AKT signaling. The upregulation of GOLPH2 was impervious in both apoV and MK-2206 groups, while MK-2206 blocks their effects in the latter, validating GOLPH2 as an upstream activator of AKT (Figure 11d). More interestingly, immunoprecipitation of AKT resulted in the coprecipitation of GOLPH2, while GOLPH2 could not be detected in allosteric AKT immunoprecipitate, confirming that exogenous GOLPH2 interacted with AKT and then modulated its phosphorylation (Figure 11e). Although it is difficult to determine a specific combination mode under existing research premises, the inhibition site of MK-2206 provides clues for further exploration.

PLT-Derived ApoVs Participate in Bone Remolding *in Vivo* via GOLPH2-AKT Signaling Axis. As for therapeutic effects in bone disorders, GOLPH2's absence and AKT signaling inhibition prevented apoVs from rescuing endogenous mMSC osteogenesis and maintaining bone homeostasis (Figure 12a−e) and discouraged apoVs from promoting bone healing (Figure 13a−d). These results illustrated that PLT-derived apoVs participated in bone regeneration via the GOLPH2-AKT signaling axis. In addition, apoVs showed superior potential compared with PLTs (Figures 12a−e, 13a−d), which have been applied in treating skeletal diseases.[70] ApoVs also possess a prominent advantage as EV functionality can be retained after going through freeze−thaw cycles, thus obviating the constrictions of storing, transporting, and applying fresh PLTs within their short shelf life.[71−73] Consequently, PLT-derived apoVs exhibit great advantage and application foreground as cell-free therapy agents.

Collectively, the above results validated that PLT-derived apoVs upregulated GOLPH2 and induced AKT phosphorylation in MSCs, adding to the knowledge on biological effects

https://doi.org/10.1021/acsnano.3c07717
ACS Nano 2023, 17, 25070−25090

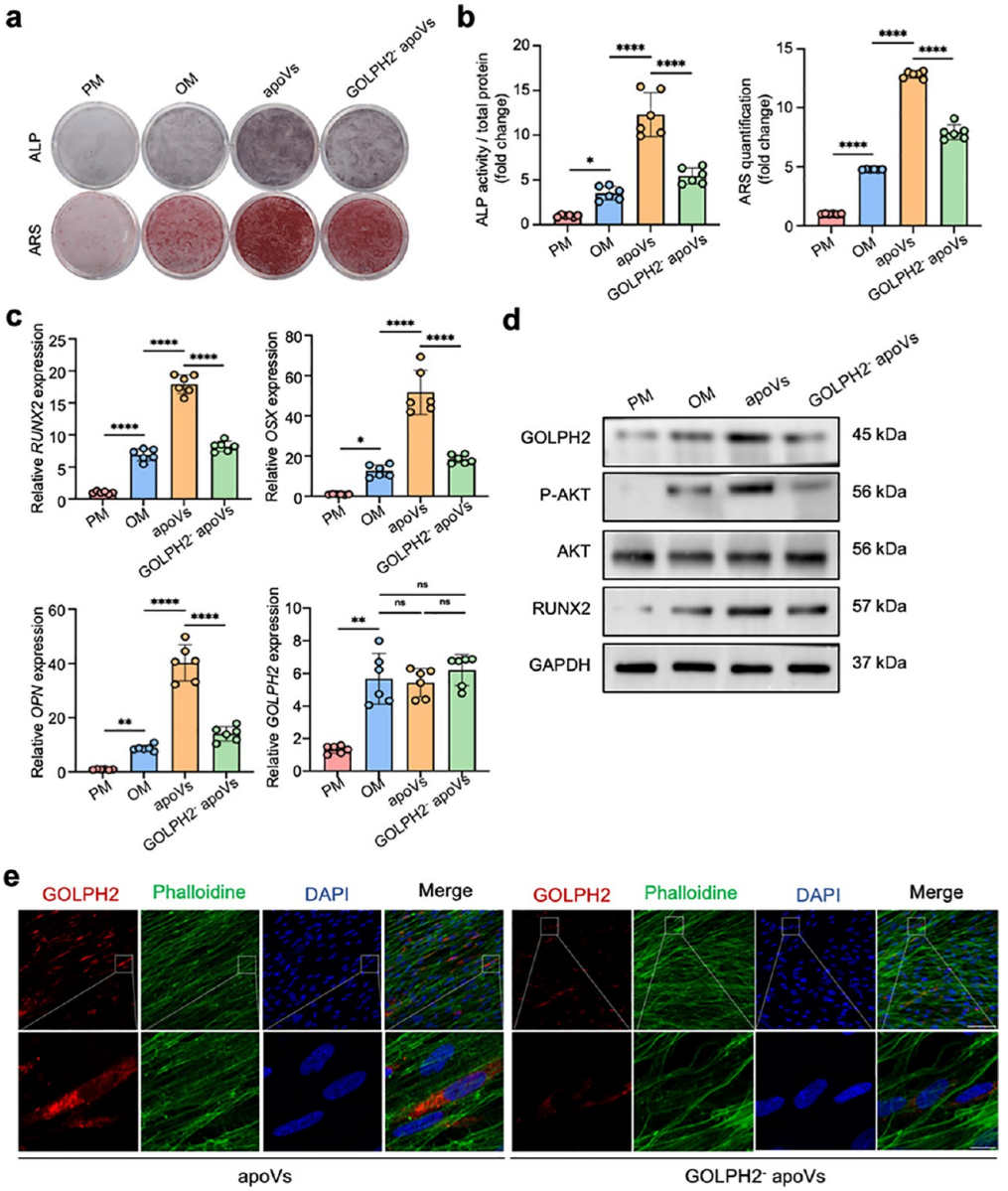

Figure 10. GOLPH2 delivery is responsible for apoV-mediated MSC osteogenesis. MSCs were cultured in PM (PM group), OM (OM group), OM with 100 ng/mL apoVs (apoV group), or GOLPH2 negative subpopulation (GOLPH2- apoV group) for 4−10 days. (a,b) ALP activities in MSCs evaluated by ALP staining and quantification. Mineralization of MSCs measured by ARS staining and quantification. (c) Expression of osteogenic genes and GOLPH2 assessed by RT-qPCR. (d) Expression of pivotal proteins detected by Western blotting. (e) Delivery of GOLPH2 showed by immunofluorescence staining. GOLPH2 in apoVs were labeled with IgG H&L (Alexa Fluor 647, red). The cytoskeleton was stained with phalloidine (green), and cell nuclei were marked with DAPI (blue). Scale bar: 100 μm (upper images), 10 μm (lower images). Data are presented as mean ± standard deviation (SD). Statistical analyses are performed by one-way ANOVA with Tukey's post hoc test or Welch's ANOVA with Dunnett's T3 post hoc test for multiple group comparisons. ns, no significant, *$p < 0.05$, **$p < 0.01$, ****$p < 0.0001$.

and mechanisms of the interaction between MSCs and apoVs. GOLPH2 insufficiency and AKT signaling silence abolished the therapeutic potential of the PLT-derived apoVs. The learning gained from our innovative applications of PLT-derived apoVs in osteoporosis and bone defects contributes to a better understanding of bone regeneration. A critical question remains as to how exogenous GOLPH2 selectively increases AKT phosphorylation. More explorations are needed to delineate the molecular mechanisms and further identify potential targets.

CONCLUSION

In this study, we provide comprehensive characteristics and proteomic landscape of PLT-derived apoVs, and we determine six proteins as specific biomarkers. Functionally, we support the recognition of PLT-derived apoVs as promising acellular therapeutic agents in the bone regeneration biomedical field, serving as a prospective method for upregulating MSC osteogenesis. Mechanically, apoVs participate in MSC osteogenesis bone remolding via GOLPH2-induced AKT phosphorylation, revealing an unrecognized apoV-MSC interaction mechanism.

EXPERIMENTAL SECTION

Reagents. All reagents and antibodies are given in Table S5.

Cell Culture. Primary human MSCs of four individuals were procured from ScienCell Company (USA). MSCs from three different

https://doi.org/10.1021/acsnano.3c07717
ACS Nano 2023, 17, 25070−25090

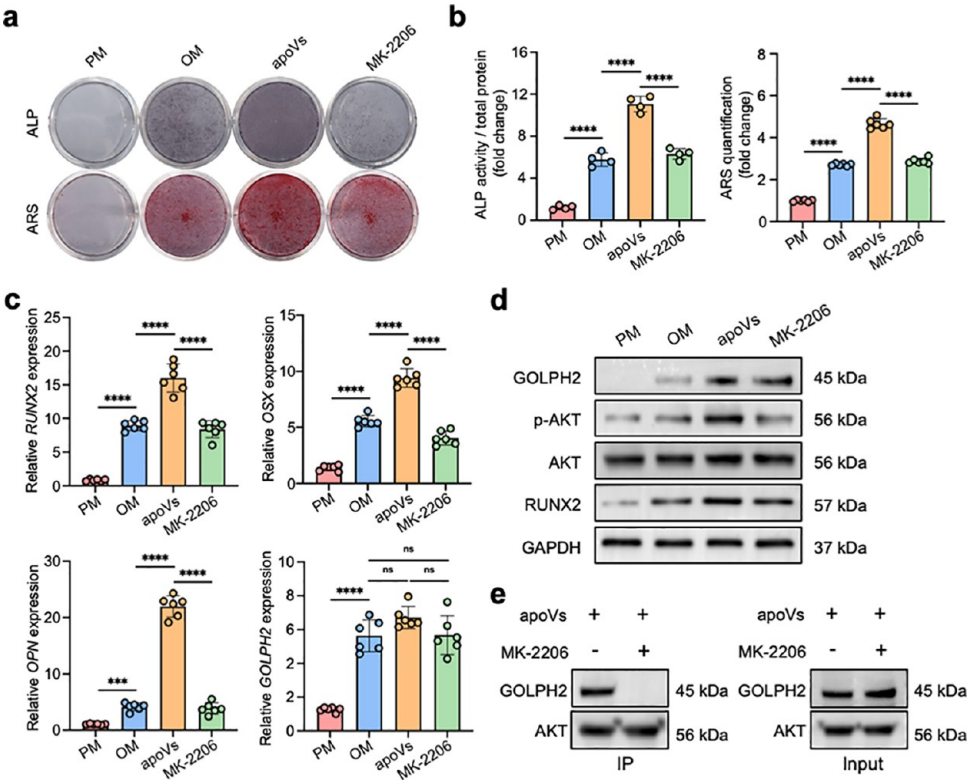

Figure 11. ApoV-mediated osteoinduction depends on GOLPH2 induced AKT phosphorylation. MSCs were cultured in PM (PM group), OM (OM group), OM with 100 ng/mL apoVs (apoV group) or apoVs and AKT allosteric inhibitor (MK-2206, MK-2206 group) for 4−10 days. (a-b) ALP stain/quantification and ARS stain/quantification of MSCs. (c) RT-qPCR analysis of osteogenic genes and GOLPH2. (d) Western blotting of pivotal proteins. (e) Co-immunoprecipitation of GOLPH2 and AKT in MSCs. Data are presented as mean ± standard deviation (SD). Statistical analyses are performed by one-way ANOVA with Tukey's post hoc test for multiple group comparisons. ns, no significant, ***$p < 0.001$, ****$p < 0.0001$.

donors were applied for cell-based studies. Primary mMSCs were separated from tibiae and femurs.[74] Cells were cultured in α-Minimum Essential Medium (α-MEM, Gibco, USA) in an incubator at 37 °C with 100% relative humidity and 5% CO_2 atmosphere. The adherent cells were digested with trypsin (Gibco, USA) and passaged *in vitro* with 80−90% confluence. The PM comprised 10% (v/v) fetal bovine serum (FBS, Gibco, USA) and 1% (v/v) penicillin/streptomycin (Gibco, USA) in α-MEM. The OM comprised 10% (v/v) FBS, 1% (v/v) penicillin/streptomycin, 10 mM β-glycerophosphate (Sigma-Aldrich, USA), 200 μM ascorbic acid (Sigma-Aldrich, USA), and 10 nM dexamethasone (Sigma-Aldrich, USA) in α-MEM.

Isolation of PLTs. The study was reviewed and approved by the Biomedical Ethics Committee of Peking University School and Hospital of Stomatology (approval code: PKUSSIRB-202170183) and conformed to the Declaration of Helsinki. All individuals who voluntarily participated in this study had given informed consent. Human whole blood was collected via venipuncture from healthy volunteers who had not taken any medication during the prior 7 days. To prevent PLT activation, we took blood into blood collection tubes with acidic citrate dextrose (ACD) via a free-flowing technique. Platelet-rich plasma (PRP) was acquired by centrifugation at 200*g* for 10 min at room temperature (RT) within 20 min of collection. PRP was separated and transferred into the polypropylene tube and suspended in 4 times the volume of Tyrode's solution (Procell, China). Prostaglandin E1 (PGE1, Sigma-Aldrich, USA) and ACD anticoagulant were added to repress PLT activation.[36] The mixture was centrifuged at 800*g* for 10 min at RT, and plasma was aspirated. PLTs were deposited at the bottom of the polypropylene tube.

Isolation of PLT-Derived ApoVs. PLTs were rinsed once with 0.1 μm-filtered phosphate-buffered saline solution (PBS) and resuspended in 500 nM staurosporine (STS, Enzo Life Sciences, USA) diluted with α-MEM. After being treated for 4 h, the medium of apoptotic PLTs (apoPLTs) was collected to isolate apoVs through sequential centrifugation and filtering.[14] Briefly, apoptotic cell debris was removed after sequential centrifugation at 800*g* for 10 min at 4 °C and once at 2000*g* for 10 min at 4 °C. ApoVs were obtained after the supernatant was gathered and followed by centrifugation at 16 000*g* for 30 min at 4 °C. Then, the apoVs were rinsed once with 0.1 μm-filtered PBS.

Scanning Electron Microscope (SEM). Samples were fixed with 4% formaldehyde (PFA) for 30 min. Samples were placed on 5 mm × 5 mm silicon wafers, after which the samples were dehydrated in ethanol, and lyophilization proceeded for 8 h.[57] Dried samples were coated with platinum (Pt). A high-resolution field emission SEM (Quanta FEG 450, FEI, USA) was used to observe morphology.

Cryo-Electron Microscopy (Cryo-EM). Based on our previous research,[14] holey-carbon grids (Quantifoil, R1.2/1.3, 300 mesh) were used to prepare Cryo-grids. Prior to sample freezing, the grids were glow-discharged for 60 s. Resuspended apoVs were deposited on those grids, and excess solution was removed by using filter paper. An FEI Vitrobot Mark IV with the setting of 100% humidity and 4 °C was applied to deal with Cryo-grids. An FEI Titan Krios TEM (Gatan K2 summit camera, USA) operated at 300 kV with a GIF quantum energy filter (Gatan, USA) was used to collect images.

Nanoparticle Tracking Analysis (NTA). For size distribution and zeta potential evaluation, apoVs were diluted in moderate 0.1 μm-filtered PBS and detected by a ZetaView PMX120 (Particle Metrix, Germany).[74] Data analysis was applied on ZetaView analysis software (Version 8.02.31).

Flow Cytometric Analysis. To determine PS exposure, samples were harvested and suspended in Annexin V binding buffer (Beyotime, China) and stained with FITC-Annexin V (Beyotime, China). Samples were kept in the dark for at least 15 min. For surface marker detection, permeabilization (Biolegend, USA) might be applied before staining (if needed). Samples were kept for at least 30 min after adding first

https://doi.org/10.1021/acsnano.3c07717
ACS Nano 2023, 17, 25070−25090

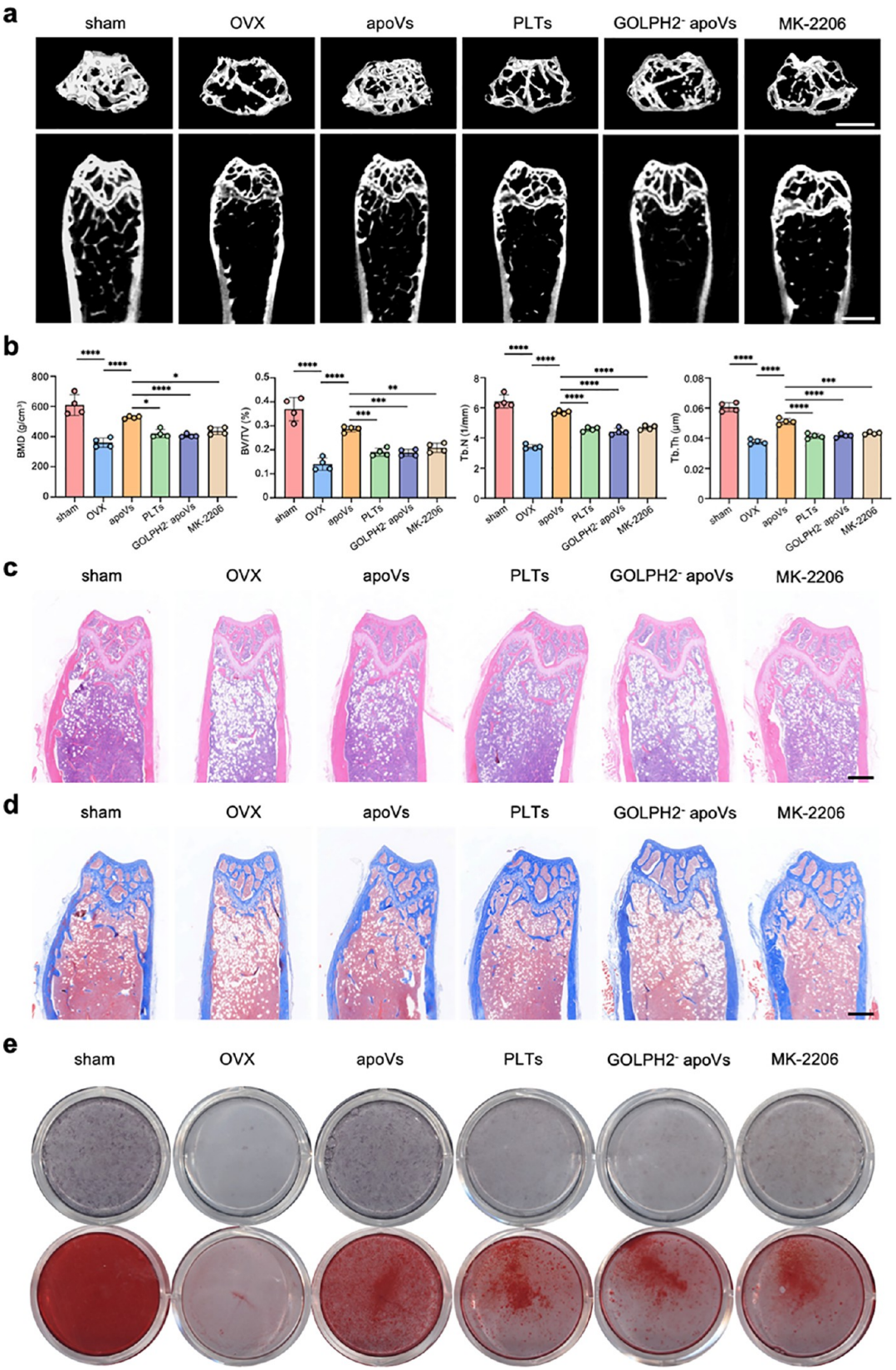

Figure 12. PLT-derived apoVs ameliorate osteoporosis via GOLPH2-AKT axis. (a) Representative 3D reconstruction images and longitudinal section images of distal femurs. Scale bar: 1 mm. (b) Bone histomorphometry of distal femurs. (c) H&E staining. Scale bar: 500 μm. (d) Masson's trichrome staining. Scale bar: 500 μm. (e) *In vitro* osteogenic differentiation ability of primary mMSCs. Data are presented as mean ± standard deviation (SD). Statistical analyses are performed by one-way ANOVA with Tukey's post hoc test or Welch's ANOVA with Dunnett's T3 post hoc test for multiple group comparisons. *$p < 0.05$, **$p < 0.01$, ***$p < 0.001$, ****$p < 0.0001$. BMD, bone mineral density; BV/TV, bone volume/total bone volume; Tb.N, trabecular number; Tb.Th, trabecular thickness.

https://doi.org/10.1021/acsnano.3c07717
ACS Nano 2023, 17, 25070−25090

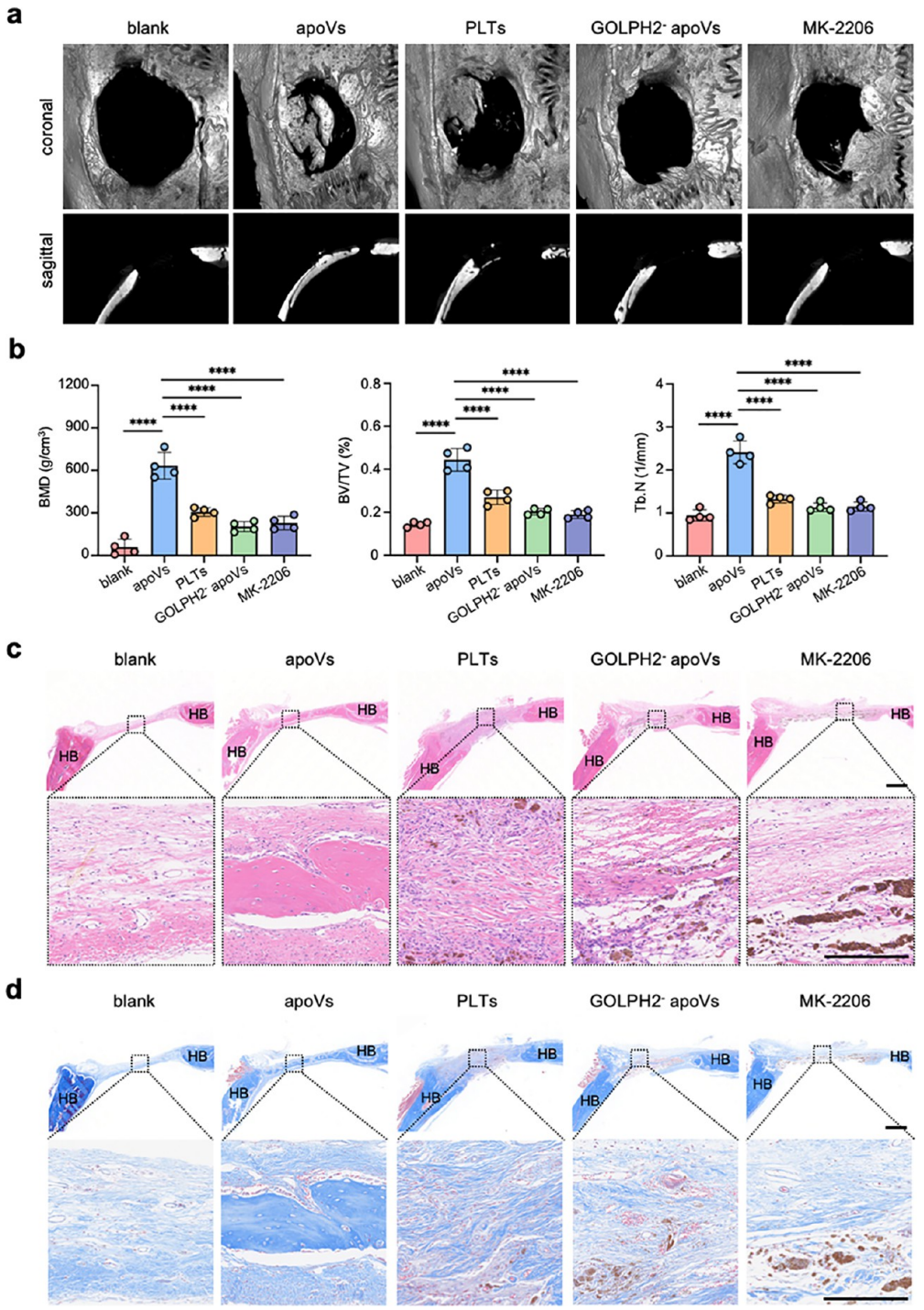

Figure 13. PLT-derived apoVs enhance bone healing in calvarial defects via GOLPH2-AKT axis. (a) Micro-CT images representing cross and sagittal sections of defects in each group. Scale bar: 1 mm. (b) Bone histomorphometry of defect areas. (c) H&E staining of the neo-generated tissues. Scale bar: 1 mm (upper images), 100 μm (lower images). (d) Masson's trichrome staining of the neo-generated tissues. Scale bar: 1 mm (upper images), 100 μm (lower images). Data are presented as mean ± standard deviation (SD). Statistical analyses are performed by one-way ANOVA with Tukey's post hoc test for multiple group comparisons. ****$p < 0.0001$. BMD, bone mineral density; BV/TV, bone volume/total bone volume; Tb.N, trabecular number; HB, host bone.

antibodies, including PE-conjugated anti-αIIbβ3 (CD41a, 1:100, Biolegend, USA), APC-conjugated anti-P-selectin (CD62P, 1:100, Invitrogen, USA), ACKR2 (1:50, Solarbio, China), CD9 (1:100, Abcam, UK), CD61 (1:100, Abcam, UK), CD81 (1:100, Abcam, UK), SEZ6L2 (1:50, ThermoFisher, USA), and GOLPH2 (1:50, Abcam, UK). The secondary antibody (PE goat antirabbit IgG (H&L), 1:500, Abcam, UK) might be used (if needed). After staining, all samples were rinsed three times using 0.5% bovine serum albumin (BSA).[75] A NovoCyte (Agilent Biosciences, USA) was used to analyze the samples. A NovoCyte (Agilent Biosciences, USA) was applied to determine the fluorescent density. The positive percentages were detected by Flowjo software (Version 10.8.1).

Immuno-Gold Labeling. Gold NPs were conjugated with the first antibody following procedures as described.[48] ApoVs were resuspended in 2% PFA and deposited on carbon-coated copper grids. The grids were rinsed with PBS and 50 mM glycine for four times separately and

https://doi.org/10.1021/acsnano.3c07717
ACS Nano 2023, 17, 25070−25090

blocked with 5% BSA for 10 min. Grids were transferred to first antibodies against CD41 (1:50, Abcam, UK), CD61 (1:50, Abcam, UK), and SEZ6L2 (1:50, ThermoFisher, USA) diluted in appropriate blocking solution and incubated for 30 min. Then, the grids were rinsed with 0.1 μm-filtered PBS eight times, rinsed with 50 mM glycine eight times, incubated in protein A-gold conjugates diluted in appropriate blocking solution for 20 min, rinsed with 0.1 μm-filtered PBS six times, incubated in 1% glutaraldehyde for 5 min, and rinsed with water six times. Transmission electron microscopy (TEM) was performed to observe the distribution of gold NPs.[76] The grids were negative stained with 1% uranyl acetate twice after drying in the air. Images were captured using a JEM1400PLUS TEM (Leica, Germany).

Proteomic Analysis. Protein lysates were formulated as antecedent described.[14] For proteomic analysis, Q-Exactive HF (Thermo Fisher Scientific, San Jose, CA) in data-dependent acquisition (DDA) mode and data-independent acquisition (DIA) mode was applied to acquire mass spectrometry (MS) data. The mixed samples went through mass spectrometry data collection in the DDA mode. MaxQuant (version 1.5.3.30) was used to analyze raw data from DDA. Each sample went through mass spectrometry data collection in DIA mode to build a library and used Spectronaut and MSstats software packages to quantify peptides and proteins. Quantitative correlation of samples, principal component analysis (PCA), and intragroup coefficient of variation (CV) were used to evaluate the quality of data. To identify proteins, both peptides and proteins were compared to the Uniprot database with a false discovery rate (FDR) set at 0.01. Proteins with fold change > = 2 and adjusted p value < 0.05 were recognized as DEPs and included for functional analysis, including KEGG category, KOG category, and GO enrichment. All of the proteins are listed in Table S1 and Table S4.

Confocal Laser Scanning Microscopy (CLSM). To observe apoV uptake, the red fluorescent cell linker PKH26 (Sigma-Aldrich, USA) was used to label apoVs.[15,77] Subsequently, MSCs were incubated with 100 ng/mL labeled apoVs for 0−72 h. The cells were triple rinsed with 0.1 μm-filtered PBS and fixed in 4% PFA for 10 min. Thereafter, the cytoskeleton was labeled with phalloidine at 5 ug/mL, and cellular nuclei were labeled with 6-diamidino-2-phenylindole (DAPI) solution (Zhong Shan-Golden Bridge Biological Technology, China) at 100 ng/mL. An LSM 5 EXCITER confocal laser scanning microscope (Carl Zeiss, Germany) was applied to capture images.

Cell Proliferation Assay. MSCs were cultured in PM and incubated with a gradient-raised concentration of apoVs. The culture media containing apoVs were replaced every 3 days. Cell-counting kit-8 (CCK-8, Dojindo, Japan) was used to estimate cell numbers following the instructions. According to the absorbance values, the cell growth curve was formulated.

ALP Staining and Quantification. To obtain ALP staining, an NBT/BCIP staining kit (CoWin Biotech, China) was applied after cell fixation. An ALP assay kit (Nanjing Jiancheng Bioengineering Institute, China) was applied to determine the ALP concentration, and a BCA protein assay was used to detect the total protein concentration in the same sample. After normalization to total protein concentrations, the final ALP activity relative to the control group was calculated.

ARS Staining and Quantification. After being fixed in 95% ethanol for 30 min, MSCs were stained with 1% ARS (pH = 4.2) at RT. Subsequently, the stains were dissolved in 100 mmol/L cetylpyridinium chloride for 30 min and mineralization quantified on the basis of absorbance value resolved at 490 nm.

RT-qPCR. Total cellular RNA was collected from MSCs with a TRIzol reagent (Invitrogen, USA). cDNA was synthesized with a PrimeScript RT Reagent Kit (Takara, Japan). RT-qPCR was conducted utilizing a 7500 Real-Time PCR Detection System (Applied Biosystems, USA) with a Power SYBR Green Master Mix (Roche, CH) following the settings: 95 °C for 10 min, 40 cycles of 95 °C for 15 s, and 60 °C for 1 min. Calculation of relative expression levels of each gene with the $2^{-\Delta\Delta CT}$ method with *GAPDH* as the internal control of quantification. Values are shown as fold changes. The primer sequences are listed in Table S6.

Protein Extraction. Whole lysates of samples were prepared as an illustration of the RIPA Lysis Buffer System (Santa Cruz Biotechnology, USA). The protein content was determined by a Pierce BCA Protein Assay Kit (Thermo Scientific, USA) per the instructions.

Western Blotting. Equal amounts of protein samples were loaded onto SDS-PAGE gel (Lablead, China) and transferred onto polyvinylidene fluoride (PVDF) membranes (Millipore, USA), which were subsequently blocked with 5% no-fat milk in TBS containing 0.1% Tween-20 (TBST) for 1 h at RT. Thereafter, the membranes were incubated with primary antibodies against CD9 (1:1000, Abcam, UK), CD81 (1:1000, Abcam, UK), TSG101 (1:1000, Abcam, UK), RhoA (1:1000, Santa Cruz Biotechnology, USA), Rab-5A (1:1000, Santa Cruz Biotechnology, USA), RPS25 (1:1000, Proteintech, USA), Fas (1:1000, Abcam, UK), ACKR2 (1:500, Solarbio, China), CD41 (1:1000, Abcam, UK), CD61 (1:1000, Abcam, UK), CD62P (1:1000, Abcam, UK), SEZ6L2 (1:1000, ThermoFisher, USA), GOLPH2 (1:1000, Abcam, UK), AKT (1:1000, Cell Signaling Technology, USA), p-AKT (1:1000, Abcam, UK) and GAPDH (1:5000, Abcam, UK) at 4 °C overnight. Subsequently, membranes were rinsed with TBST buffer and incubated with species-related peroxidase-conjugated secondary antibodies (1:10 000, Abcam, UK) for 1 h at RT. The protein bands were visualized using an ECL kit (CoWin Biotech, China) and detected by a Fusion FX6 imaging system (Vilber, France). GAPDH was used for normalization.

Lentivirus Infection. Lentiviral shRNA was applied to knockdown GOLPH2 expression in MSCs according to our previous studies.[78] MSCs were transfected with a negative control (NC) or shRNA-GOLPH2 (sh-GOLPH2; Sangon Biotech, China) following the instructions. The oligonucleotide sequences are listed in Table S7.

Magnetic-Activated ApoV Sorting. Magnetic-activated sorting was carried out as our anterior report.[14] In brief, apoVs were sequentially incubated with primary antibodies against GOLPH2 (1:1000, Abcam, UK), PE-conjugated goat antirabbit IgG (H+L) (Proteintech, USA), and anti-PE MicroBeads (Miltenyi Biotec, Germany). ApoVs were rinsed with 0.1 μm-filtered PBS between each step. Finally, apoVs were passed through a column within a magnetic field. The flow-through portion was identified as a GOLPH2-negative subpopulation, and the stranded portion was identified as a GOLPH2-positive subpopulation.

Immunofluorescence. ApoVs were permeabilizated (Biolegend, USA) for 3−5 min and rinsed five times in 0.1 μm-filtered PBS at 16 000g for 30 min. Next, apoVs were incubated in the first antibody (GOLPH2, 1:50, Abcam, UK) overnight at 4 °C and rinsed two times. After apoVs were stained with IgG H&L (Alexa Fluor 647, Abcam, UK) for 1−2 h and rinsed two times, MSCs were incubated with those apoVs for 24 h. The remaining steps refer to CLSM.

Immunoprecipitation Assays. ApoVs were collected and lysed in a Nonidet P-40 buffer together with a complete protease inhibitor mixture. Generally, 4−6 μg of antibodies were incubated with around 800 mg of cell lysates at 4 °C for 8−12 h. Afterward, protein A/G-agarose beads were added in the lysates and incubated with cell lysates at 4 °C for 2−4 h. Then, the immunoprecipitations were rinsed in lysis buffer and eluted with 2 × SDS loading buffer through boiling for 5 min at 99 °C. The remaining steps refer to Western blotting.

Animals. All animals were purchased from Vital River (China). Animals were kept in a specific-pathogen-free environment with a 12 h light-dark cycle and a RT of 23 ± 3 °C at the Peking University School and Hospital of Stomatology. Animals had free access to sterilized maintenance diets and autoclaved water. The Institutional Animal Care and Use Committee of the Peking University Health Science Center approved all animal experiments in this study according to institutional animal guidelines (permit number: LA 2022039).

Heterotopic Bone Formation Assay *in Vivo*. Subcutaneous implantation of MSCs in BALB/c nude mice was implemented our anterior report.[79] Briefly, 1 × 10^6 cells were trypsinized and resuspended, mixed with β-TCP (Bicon, USA) particles, and placed in cryotubes. To facilitate cell adhesion, the mixtures were placed in a shaker at 37 °C for 1 h and centrifuged at 1000g for 5 min. Afterward, the scaffolds were implanted into 8-week-old female BALB/c nude mice. After 8 weeks of implantation, the implants were harvested, fixed in 4% PFA for 24 h, decalcified in 10% ethylene diamine tetra-acetic

https://doi.org/10.1021/acsnano.3c07717
ACS Nano 2023, 17, 25070−25090

acid (EDTA, pH = 7.4) for 14 days, and embedded in paraffin after dehydration. The specimens were sliced and histological staining.

Intravenous Injection of ApoVs in OVX Mice. An OVX mouse model was implemented according to previous studies.[80] Female eight week old C57BL/6J mice were randomly subjected to bilateral oophorectomy and sham operation. Three months postoperation, tail intravenous injection of apoVs was administered once a week, using the equivalent vehicle (0.1 μm-filtered PBS) as a control. Three months after supplementation, all mice were killed after being anesthetized. Viscera and femurs were harvested. Viscera and left femurs were fixed in 4% PFA for 1 week. To estimate the bone mass and microarchitecture, micro-CT was executed by an Inveon microcomputed tomography (Siemens, Germany) according to the following settings: 220 μA node current, 60 kV X-ray voltage, and 1500 ms exposure time for each of 360 rotational steps. BMD and bone morphometric parameters were determined by an Inveon Research Workplace (Siemens, Germany) based on common guidelines.[81] Thereafter, the samples were decalcified, embedded, sliced, and analyzed by histological staining.

Implantation of ApoVs in Calvarial Critical-Size Defects in Rats. PLGA/pDA scaffold preparation was implemented as reported previously.[57] PLGA/pDA scaffolds were immersed in apoV solution at 4 °C for 12 h. To observe the distribution of apoVs on scaffolds, apoVs were labeled with PKH26, and confocal images were captured. To measure apoV release after immobilization, we incubated the compound materials in saline at 37 °C and collected supernatants at predetermined time intervals of 1−14 days. BCA protein assay was applied to determine the protein content of released apoVs. *In situ*, calvarial defects (5 mm diameter) in Sprague−Dawley rats were constructed using a trephine bur with copious saline irrigation. PLAG/pDA scaffolds loaded apoVs were implanted in defects, with no scaffold and PLAG/pDA scaffolds as control. Eight weeks postoperation, viscera and the whole calvarium were harvested. Samples were fixed in 4% PFA for 1 week. To assess bone formation, micro-CT was executed by an Inveon microcomputed tomography (Siemens, Germany) according to the settings: 500 μA node current, 80 kV X-ray voltage, and 1500 ms exposure time for each of 360 rotational steps. BMD and bone morphometric parameters were determined by an Inveon Research Workplace (Siemens, Germany) based on common guidelines.[81] Thereafter, the samples were subjected to histological examination.

Statistical Analysis. Data from three or more independent experiments are presented as mean ± standard deviation (SD). Results were analyzed by SPSS 20.0 software (IBM, USA). Comparisons between two groups were analyzed by independent two-tailed Student's *t* test or two-tailed Student's *t* test with Welch correction. Comparisons among multiple groups were analyzed by one-way ANOVA followed by Turkey's post hoc test or Welch's ANOVA with Dunnett's T3 post hoc test. Values of $p < 0.05$ were considered statistically significant.

ASSOCIATED CONTENT

Data Availability Statement

The data that support the findings of this study are available from the corresponding author upon reasonable request.

Supporting Information

The Supporting Information is available free of charge at https://pubs.acs.org/doi/10.1021/acsnano.3c07717.

Figure S1. The size distribution of isolated PLTs. Figure S2. The optimal condition for collecting PLT-derived apoVs *in vitro*. Figure S3. Biosafety of PLT-derived apoVs *in vitro*. Figure S4. MSCs endocytose PLT-derived apoVs. Figure S5. Active concentration of PLT-derived apoVs for MSC osteogenic induction. Figure S6. Biodistribution of PLT-derived apoVs. Figure S7. Biosafety of PLT-derived apoVs in mice. Figure S8. Characterization of engineered PLGA/pDA-apoVs compounds. Figure S9. Biosafety of PLT-derived apoVs in rats. Figure S10. Autogenous PLT-derived apoVs facilitate bone healing of critical-sized defect. Figure S11. Functional categories of DEPs between MSCs with or without apoV induction. Figure S12. GO enrichment of DEPs between MSCs with or without apoV induction. Figure S13. GOLPH2 deficiency downregulate MSC osteogenesis. Figure S14. Sorting of GOLPH2-negative apoV subpopulation. Figure S15. PLT-derived apoVs enhance MSCs osteogenesis *in vivo* via GOLPH2-AKT axis (DOCX)

Table S1. List of all the proteins quantified during proteomic analysis of PLTs and apoVs (XLSX)

Table S2. List of the top 100 upregulated proteins in apoVs compared to PLTs (XLS)

Table S3. List of the top 100 downregulated proteins in apoVs compared to PLTs (XLS)

Table S4. List of all the proteins quantified during proteomic analysis of MSCs with or without apoV induction (XLSX)

Table S5. Reagents and antibodies (XLSX)

Table S6. Primers for qRT-PCR (XLSX)

Table S7. Sequences of shRNA (XLSX)

AUTHOR INFORMATION

Corresponding Authors

Xiao Zhang − *Department of Prosthodontics, Peking University School and Hospital of Stomatology, National Center of Stomatology, National Clinical Research Center for Oral Disease, National Engineering Research Center of Oral Biomaterials and Digital Medical Devices, Beijing Key Laboratory of Digital Stomatology, Research Center of Engineering and Technology for Computerized Dentistry Ministry of Health, NMPA Key Laboratory for Dental Materials, Beijing 100081, China*; Email: kqxiaozhang@hsc.pku.edu.cn

Yongsheng Zhou − *Department of Prosthodontics, Peking University School and Hospital of Stomatology, National Center of Stomatology, National Clinical Research Center for Oral Disease, National Engineering Research Center of Oral Biomaterials and Digital Medical Devices, Beijing Key Laboratory of Digital Stomatology, Research Center of Engineering and Technology for Computerized Dentistry Ministry of Health, NMPA Key Laboratory for Dental Materials, Beijing 100081, China*; orcid.org/0000-0002-4332-0878; Email: kqzhouysh@hsc.pku.edu.cn

Authors

Yuhe Jiang − *Department of Prosthodontics, Peking University School and Hospital of Stomatology, National Center of Stomatology, National Clinical Research Center for Oral Disease, National Engineering Research Center of Oral Biomaterials and Digital Medical Devices, Beijing Key Laboratory of Digital Stomatology, Research Center of Engineering and Technology for Computerized Dentistry Ministry of Health, NMPA Key Laboratory for Dental Materials, Beijing 100081, China*

Yuan Zhu − *Department of Prosthodontics, Peking University School and Hospital of Stomatology, National Center of Stomatology, National Clinical Research Center for Oral Disease, National Engineering Research Center of Oral Biomaterials and Digital Medical Devices, Beijing Key Laboratory of Digital Stomatology, Research Center of Engineering and Technology for Computerized Dentistry Ministry of Health, NMPA Key Laboratory for Dental Materials, Beijing 100081, China*

https://doi.org/10.1021/acsnano.3c07717
ACS Nano 2023, 17, 25070−25090

Yuzi Shao − *Department of Prosthodontics, Peking University School and Hospital of Stomatology, National Center of Stomatology, National Clinical Research Center for Oral Disease, National Engineering Research Center of Oral Biomaterials and Digital Medical Devices, Beijing Key Laboratory of Digital Stomatology, Research Center of Engineering and Technology for Computerized Dentistry Ministry of Health, NMPA Key Laboratory for Dental Materials, Beijing 100081, China*

Kunkun Yang − *Department of Prosthodontics, Peking University School and Hospital of Stomatology, National Center of Stomatology, National Clinical Research Center for Oral Disease, National Engineering Research Center of Oral Biomaterials and Digital Medical Devices, Beijing Key Laboratory of Digital Stomatology, Research Center of Engineering and Technology for Computerized Dentistry Ministry of Health, NMPA Key Laboratory for Dental Materials, Beijing 100081, China*

Lei Zhu − *Department of Prosthodontics, Peking University School and Hospital of Stomatology, National Center of Stomatology, National Clinical Research Center for Oral Disease, National Engineering Research Center of Oral Biomaterials and Digital Medical Devices, Beijing Key Laboratory of Digital Stomatology, Research Center of Engineering and Technology for Computerized Dentistry Ministry of Health, NMPA Key Laboratory for Dental Materials, Beijing 100081, China*

Yunsong Liu − *Department of Prosthodontics, Peking University School and Hospital of Stomatology, National Center of Stomatology, National Clinical Research Center for Oral Disease, National Engineering Research Center of Oral Biomaterials and Digital Medical Devices, Beijing Key Laboratory of Digital Stomatology, Research Center of Engineering and Technology for Computerized Dentistry Ministry of Health, NMPA Key Laboratory for Dental Materials, Beijing 100081, China;* orcid.org/0000-0001-8364-1898

Ping Zhang − *Department of Prosthodontics, Peking University School and Hospital of Stomatology, National Center of Stomatology, National Clinical Research Center for Oral Disease, National Engineering Research Center of Oral Biomaterials and Digital Medical Devices, Beijing Key Laboratory of Digital Stomatology, Research Center of Engineering and Technology for Computerized Dentistry Ministry of Health, NMPA Key Laboratory for Dental Materials, Beijing 100081, China*

Complete contact information is available at: https://pubs.acs.org/10.1021/acsnano.3c07717

Author Contributions

Yuhe Jiang designed and performed most of the *in vitro* and *in vivo* experiments, analyzed the data, and wrote the manuscript. Yuan Zhu and Yuzi Shao contributed to PLT-derived apoVs isolation and characterization. Yang Kunkun and Lei Zhu performed part of the *in vitro* experiments and discussed the results. Yunsong Liu and Ping Zhang designed part of the *in vivo* experiments. Yongsheng Zhou and Xiao Zhang designed the project, provided technical and resource assistance, and revised the manuscript.

Funding

This work was supported by grants from the Beijing Natural Science Foundation (grant number 7222224), the Nation Natural Science Foundation of China (grant number 81930026), and the Clinical Research Foundation of Peking University School and Hospital of Stomatology (grant number PKUSS-2023CRF1005).

Notes

The authors declare no competing financial interest.

ACKNOWLEDGMENTS

The authors thank the Core Facilities of Life Sciences, Peking University for assistance with immuno-gold labeling and SEM, and we are grateful to Yiqun Liu for his help with immuno-gold labeling and Rui Jiao for her help in making EM samples. Cryo-EM data were collected on the Electron Microscopy Laboratory of Peking University with the assistance of Xuemei Li. Micro-CT evaluation service was provided by Wen Zhou at Peking University School of Stomatology. The authors acknowledge the use of Biorender to create schematic figure in this paper.

REFERENCES

(1) Kerr, J. F.; Wyllie, A. H.; Currie, A. R. Currie. Apoptosis: a Basic Biological Phenomenon with Wide-Ranging Implications in Tissue Kinetics. *Br. J. Cancer* **1972**, *26*, 239−257.

(2) Bergmann, A.; Steller, H. Apoptosis, Stem Cells, and Tissue Regeneration. *Sci. Signal* **2010**, *3*, re8.

(3) Fuchs, Y.; Steller, H. Programmed Cell Death in Animal Development and Disease. *Cell* **2011**, *147*, 742−758.

(4) Ye, Q.; Xu, H.; Liu, S.; Li, Z.; Zhou, J.; Ding, F.; Zhang, X.; Wang, Y.; Jin, Y.; Wang, Q. Apoptotic Extracellular Vesicles Alleviate Pg-LPS Induced Inflammatory Responses of Macrophages via AMPK/SIRT1/NF-κB Pathway and Inhibit Osteoclast Formation. *J. Periodontol* **2022**, *93*, 1738−1751.

(5) Wang, J.; Cao, Z.; Wang, P.; Zhang, X.; Tang, J.; He, Y.; Huang, Z.; Mao, X.; Shi, S.; Kou, X. Apoptotic Extracellular Vesicles Ameliorate Multiple Myeloma by Restoring Fas-Mediated Apoptosis. *ACS Nano* **2021**, *15*, 14360−14372.

(6) Liu, G.; Yin, X. M. The Role of Extracellular Vesicles in Liver Pathogenesis. *Am. J. Pathol.* **2022**, *192*, 1358−1367.

(7) Zheng, C.; Sui, B.; Zhang, X.; Hu, J.; Chen, J.; Liu, J.; Wu, D.; Ye, Q.; Xiang, L.; Qiu, X.; Liu, S.; Deng, Z.; Zhou, J.; Liu, S.; Shi, S.; Jin, Y. Apoptotic Vesicles Restore Liver Macrophage Homeostasis to Counteract Type 2 Diabetes. *J. Extracell. Vesicles* **2021**, *10*, No. e12109.

(8) Paone, S.; Baxter, A. A.; Hulett, M. D.; Poon, I. K. H. Endothelial Cell Apoptosis and the Role of Endothelial Cell-Derived Extracellular Vesicles in the Progression of Atherosclerosis. *Cell. Mol. Life Sci.* **2019**, *76*, 1093−1106.

(9) Ou, Q.; Tan, L.; Shao, Y.; Lei, F.; Huang, W.; Yang, N.; Qu, Y.; Cao, Z.; Niu, L.; Liu, Y.; Kou, X.; Shi, S. Electrostatic Charge-Mediated Apoptotic Vesicle Biodistribution Attenuates Sepsis by Switching Neutrophil NETosis to Apoptosis. *Small* **2022**, *18*, No. e2200306.

(10) Shao, Y.; Jiang, Y.; Yang, K.; Zhu, Y.; Liu, Y.; Zhang, P.; Lv, L.; Zhang, X.; Zhou, Y. Apoptotic Vesicles Derived from Human Red Blood Cells Promote Bone Regeneration via Carbonic Anhydrase 1. *Cell Prolif.* **2023**, *11*, No. e13547.

(11) Ye, Q.; Qiu, X.; Wang, J.; Xu, B.; Su, Y.; Zheng, C.; Gui, L.; Yu, L.; Kuang, H.; Liu, H.; He, X.; Ma, Z.; Wang, Q.; Jin, Y. MSCs-Derived Apoptotic Extracellular Vesicles Promote Muscle Regeneration by Inducing Pannexin 1 Channel-Dependent Creatine Release by Myoblasts. *Int. J. Oral Sci.* **2023**, *15*, 7.

(12) Liu, J.; Qiu, X.; Lv, Y.; Zheng, C.; Dong, Y.; Dou, G.; Zhu, B.; Liu, A.; Wang, W.; Zhou, J.; Liu, S.; Liu, S.; Gao, B.; Jin, Y. Apoptotic Bodies Derived From Mesenchymal Stem Cells Promote Cutaneous Wound Healing via Regulating the Functions of Macrophages. *Stem Cell Res. Ther.* **2020**, *11*, 507.

(13) Bussolati, B.; Camussi, G. Renal Injury: Early Apoptotic Extracellular Vesicles in Injury and Repair. *Nat. Rev. Nephrol.* **2017**, *13*, 523−524.

(14) Zhang, X.; Tang, J.; Kou, X.; Huang, W.; Zhu, Y.; Jiang, Y.; Yang, K.; Li, C.; Hao, M.; Qu, Y.; Ma, L.; Chen, C.; Shi, S.; Zhou, Y. Proteomic Analysis of MSC-Derived Apoptotic Vesicles Identifies Fas Inheritance to Ameliorate Haemophilia A via Activating Platelet Functions. *J. Extracell. Vesicles* **2022**, *11*, No. e12240.
(15) Zhu, Y.; Yang, K.; Cheng, Y.; Liu, Y.; Gu, R.; Liu, X.; Liu, H.; Zhang, X.; Liu, Y. Apoptotic Vesicles Regulate Bone Metabolism via the MiR1324/SNX14/SMAD1/5 Signaling Axis. *Small* **2023**, *19*, No. e2205813.
(16) Zhu, L.; Sun, H. T.; Wang, S.; Huang, S. L.; Zheng, Y.; Wang, C. Q.; Hu, B. Y.; Qin, W.; Zou, T. T.; Fu, Y.; Shen, X. T.; Zhu, W. W.; Geng, Y.; Lu, L.; Jia, H. L.; Qin, L. X.; Dong, Q. Z. Isolation and Characterization of Exosomes for Cancer Research. *J. Hematol. Oncol.* **2020**, *13*, 152.
(17) Patel, D. B.; Gray, K. M.; Santharam, Y.; Lamichhane, T. N.; Stroka, K. M.; Jay, S. M. Impact of Cell Culture Parameters on Production and Vascularization Bioactivity of Mesenchymal Stem Cell-Derived Extracellular Vesicles. *Bioeng. Transl. Med.* **2017**, *2*, 170−179.
(18) Malkin, E. Z.; Bratman, S. V. Bioactive DNA from Extracellular Vesicles and Particles. *Cell Death Dis.* **2020**, *11*, 584.
(19) Elzanowska, J.; Semira, C.; Costa-Silva, B. DNA in Extracellular Vesicles: Biological and Clinical Aspects. *Mol. Oncol.* **2021**, *15*, 1701−1714.
(20) Xu, F.; Fei, Z.; Dai, H.; Xu, J.; Fan, Q.; Shen, S.; Zhang, Y.; Ma, Q.; Chu, J.; Peng, F.; Zhou, F.; Liu, Z.; Wang, C. Mesenchymal Stem Cell-Derived Extracellular Vesicles with High PD-L1 Expression for Autoimmune Diseases Treatment. *Adv. Mater.* **2022**, *34*, No. e2106265.
(21) Xu, L.; Liang, Y.; Xu, X.; Xia, J.; Wen, C.; Zhang, P.; Duan, L. Blood Cell-Derived Extracellular Vesicles: Diagnostic Biomarkers and Smart Delivery Systems. *Bioengineered* **2021**, *12*, 7929−7940.
(22) Lebois, M.; Josefsson, E. C. Regulation of Platelet Lifespan by Apoptosis. *Platelets* **2016**, *27*, 497−504.
(23) Yáñez-Mó, M.; Siljander, P. R.; Andreu, Z.; Bedina Zavec, A. B.; Borràs, F. E.; Buzas, E. I.; Buzas, K.; Casal, E.; Cappello, F.; Carvalho, J.; Colás, E.; Cordeiro-da Silva, A.; Fais, S.; Falcon-Perez, J. M.; Ghobrial, I. M.; Giebel, B.; Gimona, M.; Graner, M.; Gursel, I.; Gursel, M.; et al. Biological Properties of Extracellular Vesicles and Their Physiological Functions. *J. Extracell. Vesicles* **2015**, *4*, 27066.
(24) Rondina, M. T.; Schwertz, H.; Harris, E. S.; Kraemer, B. F.; Campbell, R. A.; Mackman, N.; Grissom, C. K.; Weyrich, A. S.; Zimmerman, G. A. The Septic Milieu Triggers Expression of Spliced Tissue Factor mRNA in Human Platelets. *J. Thromb. Haemost.* **2011**, *9*, 748−758.
(25) Lopez, E.; Srivastava, A. K.; Burchfield, J.; Wang, Y. W.; Cardenas, J. C.; Togarrati, P. P.; Miyazawa, B.; Gonzalez, E.; Holcomb, J. B.; Pati, S.; Wade, C. E. Platelet-Derived Extracellular Vesicles Promote Hemostasis and Prevent the Development of Hemorrhagic Shock. *Sci. Rep.* **2019**, *9*, 17676.
(26) Li, Q.; Huang, Z.; Wang, Q.; Gao, J.; Chen, J.; Tan, H.; Li, S.; Wang, Z.; Weng, X.; Yang, H.; Pang, Z.; Song, Y.; Qian, J.; Ge, J. Targeted Immunomodulation Therapy for Cardiac Repair by Platelet Membrane Engineering Extracellular Vesicles via Hitching Peripheral Monocytes. *Biomaterials* **2022**, *284*, 121529.
(27) Adamczyk, A. M.; Leicaj, M. L.; Fabiano, M. P.; Cabrerizo, G.; Bannoud, N.; Croci, D. O.; Witwer, K. W.; Remes Lenicov, F.; Ostrowski, M.; Perez, P. S. Extracellular Vesicles from Human Plasma Dampen Inflammation and Promote Tissue Repair Functions in Macrophages. *J. Extracell. Vesicles* **2023**, *12*, No. e12331.
(28) Żmigrodzka, M.; Witkowska-Piłaszewicz, O.; Winnicka, A. Platelets Extracellular Vesicles as Regulators of Cancer Progression-An Updated Perspective. *Int. J. Mol. Sci.* **2020**, *21*, 5195.
(29) Kim, H. K.; Song, K. S.; Chung, J. H.; Lee, K. R.; Lee, S. N. Platelet Microparticles Induce Angiogenesis in vitro. *Br. J. Hamaetol.* **2004**, *124*, 376−384.
(30) Brill, A.; Dashevsky, O.; Rivo, J.; Gozal, Y.; Varon, D. Platelet-Derived Microparticles Induce Angiogenesis and Stimulate Post-Ischemic Revascularization. *Cardiovasc. Res.* **2005**, *67*, 30−38.
(31) Hayon, Y.; Dashevsky, O.; Shai, E.; Varon, D.; Leker, R. R. Platelet Microparticles Promote Neural Stem Cell Proliferation, Survival and Differentiation. *Journal of Molecular Neuroscience* **2012**, *47*, 659−665.
(32) Hayon, Y.; Dashevsky, O.; Shai, E.; Brill, A.; Varon, D.; Leker, R. R. Platelet Microparticles Induce Angiogenesis and Neurogenesis after Cerebral Ischemia. *Current Neurovascular Research* **2012**, *9*, 185−192.
(33) Iyer, S. R.; Scheiber, A. L.; Yarowsky, P.; Henn, R. F., 3rd.; Otsuru, S.; Lovering, R. M. Exosomes Isolated from Platelet-Rich Plasma and Mesenchymal Stem Cells Promote Recovery of Function After Muscle Injury. *Am. J. Sports Med.* **2020**, *48*, 2277−2286.
(34) Gardiner, C.; Di Vizio, D.; Sahoo, S.; Thery, C.; Witwer, K. W.; Wauben, M.; Hill, A. F. Techniques Used for the Isolation and Characterization of Extracellular Vesicles: Results of a Worldwide Survey. *J. Extracell. Vesicles* **2016**, *5*, 32945.
(35) Mcarthur, K.; Chappaz, S.; Kile, B. T. Apoptosis in Megakaryocytes and Platelets: the Life and Death of a Lineage. *Blood* **2018**, *131*, 605−610.
(36) Aatonen, M. T.; Ohman, T.; Nyman, T. A.; Laitinen, S.; Grönholm, M.; Siljander, P. R. Isolation and Characterization of Platelet-Derived Extracellular Vesicles. *J. Extracell. Vesicles* **2014**, *3*, 24692.
(37) Barkalow, F. J.; Barkalow, K. L.; Mayadas, T. N. Dimerization of P-Selectin in Platelets and Endothelial Cells. *Blood* **2000**, *96*, 3070−3077.
(38) Thon, J. N.; Italiano, J. E. Platelets: Production, Morphology and Ultrastructure. *Handb. Exp. Pharmacol.* **2012**, *210*, 3−22.
(39) Frelinger, A. L., 3RD. Using Flow Cytometry to Monitor Glycoprotein IIb-IIIa Activation. *Platelets* **2018**, *29*, 670−676.
(40) Blair, T. A.; Frelinger, A. L., 3RD. Platelet Surface Marker Analysis by Mass Cytometry. *Platelets* **2020**, *31*, 633−640.
(41) Théry, C.; Witwer, K. W.; Aikawa, E.; Alcaraz, M. J.; Anderson, J. D.; Andriantsitohaina, R.; Antoniou, A.; Arab, T.; Archer, F.; Atkin-Smith, G. K.; Ayre, D. C.; Bach, J. M.; Bachurski, D.; Baharvand, H.; Balaj, L.; Baldacchino, S.; Bauer, N. N.; Baxter, A. A.; Bebawy, M.; Beckham, C.; et al. Minimal Information for Studies of Extracellular Vesicles 2018 (MISEV2018): a Position Statement of the International Society for Extracellular Vesicles and Update of the MISEV2014 Guidelines. *J. Extracell. Vesicles* **2018**, *7*, 1535750.
(42) Crescitelli, R.; Lässer, C.; Szabó, T. G.; Kittel, A.; Eldh, M.; Dianzani, I.; Buzás, E. I.; Lötvall, J. Distinct RNA Profiles in Subpopulations of Extracellular Vesicles: Apoptotic Bodies, Microvesicles and Exosomes. *J. Extracell. Vesicles* **2013**, *2*, 20677.
(43) Mustard, J. F.; Rowsell, H. C.; Murphy, E. A. Platelet Economy (Platelet Survival and Turnover). *Br. J. Hamaetol.* **1966**, *12*, 1−24.
(44) Mason, K. D.; Carpinelli, M. R.; Fletcher, J. I.; Collinge, J. E.; Hilton, A. A.; Ellis, S.; Kelly, P. N.; Ekert, P. G.; Metcalf, D.; Roberts, A. W.; Huang, D. C.; Kile, B. T. Programmed Anuclear Cell Death Delimits Platelet Life Span. *Cell* **2007**, *128*, 1173−1186.
(45) Suzuki, J.; Umeda, M.; Sims, P. J.; Nagata, S. Calcium-Dependent Phospholipid Scrambling by TMEM16F. *Nature* **2010**, *468*, 834−838.
(46) Suzuki, J.; Denning, D. P.; Imanishi, E.; Horvitz, H. R.; Nagata, S. Xk-Related Protein 8 and CED-8 Promote Phosphatidylserine Exposure in Apoptotic Cells. *Science* **2013**, *341*, 403−406.
(47) Wang, J.; Cao, Z.; Wang, P.; Zhang, X.; Tang, J.; He, Y.; Huang, Z.; Mao, X.; Shi, S.; Kou, X. Apoptotic Extracellular Vesicles Ameliorate Multiple Myeloma by Restoring Fas-Mediated Apoptosis. *ACS Nano* **2021**, *15*, 14360−14372.
(48) Brisson, A. R.; Tan, S.; Linares, R.; Gounou, C.; Arraud, N. Extracellular Vesicles from Activated Platelets: a Semiquantitative Cryo-electron Microscopy and Immuno-Gold Labeling Study. *Platelets* **2017**, *28*, 263−271.
(49) Kang, M.; Jordan, V.; Blenkiron, C.; Chamley, L. W. Biodistribution of Extracellular Vesicles Following Administration into Animals: a Systematic Review. *J. Extracell. Vesicles* **2021**, *10*, No. e12085.
(50) Qing, S.; Lyu, C.; Zhu, L.; Pan, C.; Wang, S.; Li, F.; Wang, J.; Yue, H.; Gao, X.; Jia, R.; Wei, W.; Ma, G. Biomineralized Bacterial Outer Membrane Vesicles Potentiate Safe and Efficient Tumor Microenvironment Reprogramming for Anticancer Therapy. *Adv. Mater.* **2020**, *32*, No. e2002085.

https://doi.org/10.1021/acsnano.3c07717
ACS Nano 2023, 17, 25070−25090

(51) Liao, Z.; Liu, H.; Ma, L.; Lei, J.; Tong, B.; Li, G.; Ke, W.; Wang, K.; Feng, X.; Hua, W.; Li, S.; Yang, C. Engineering Extracellular Vesicles Restore the Impaired Cellular Uptake and Attenuate Intervertebral Disc Degeneration. *ACS Nano* **2021**, *15*, 14709−14724.
(52) Nishimura, T.; Sasaki, Y.; Akiyoshi, K. Biotransporting Self-Assembled Nanofactories Using Polymer Vesicles with Molecular Permeability for Enzyme Prodrug Cancer Therapy. *Adv. Mater.* **2017**, *29*, 1702406.
(53) Hu, S.; Li, Z.; Cores, J.; Huang, K.; Su, T.; Dinh, P. U.; Cheng, K. Needle-Free Injection of Exosomes Derived from Human Dermal Fibroblast Spheroids Ameliorates Skin Photoaging. *ACS Nano* **2019**, *13*, 11273−11282.
(54) Li, X.; Zhu, T.; Wang, R.; Chen, J.; Tang, L.; Huo, W.; Huang, X.; Cao, Q. Genetically Programmable Vesicles for Enhancing CAR-T Therapy against Solid Tumors. *Adv. Mater.* **2023**, *35*, No. e2211138.
(55) Feng, Q.; Ma, X.; Cheng, K.; Liu, G.; Li, Y.; Yue, Y.; Liang, J.; Zhang, L.; Zhang, T.; Wang, X.; Gao, X.; Nie, G.; Zhao, X. Engineered Bacterial Outer Membrane Vesicles as Controllable Two-Way Adaptors to Activate Macrophage Phagocytosis for Improved Tumor Immunotherapy. *Adv. Mater.* **2022**, *34*, No. e2206200.
(56) Zhang, X.; Zhang, H.; Gu, J.; Zhang, J.; Shi, H.; Qian, H.; Wang, D.; Xu, W.; Pan, J.; Santos, H. A. Engineered Extracellular Vesicles for Cancer Therapy. *Adv. Mater.* **2021**, *33*, No. e2005709.
(57) Li, W.; Liu, Y.; Zhang, P.; Tang, Y.; Zhou, M.; Jiang, W.; Zhang, X.; Wu, G.; Zhou, Y. Tissue-Engineered Bone Immobilized with Human Adipose Stem Cells-Derived Exosomes Promotes Bone Regeneration. *ACS Appl. Mater. Interfaces* **2018**, *10*, 5240−5254.
(58) Agliarulo, I.; Parashuraman, S. Golgi Apparatus Regulates Plasma Membrane Composition and Function. *Cells* **2022**, *11*, 368.
(59) Denais, C.; Dent, C. L.; Southgate, L.; Hoyle, J.; Dafou, D.; Trembath, R. C.; Machado, R. D. Dymeclin, the Gene Underlying Dyggve-Melchior-Clausen Syndrome, Encodes a Protein Integral to Extracellular Matrix and Golgi Organization and is Associated with Protein Secretion Pathways Critical in Bone Development. *Hum. Mutat.* **2011**, *32*, 231−239.
(60) Yan, G.; Ru, Y.; Wu, K.; Yan, F.; Wang, Q.; Wang, J.; Pan, T.; Zhang, M.; Han, H.; Li, X.; Zou, L. GOLM1 Promotes Prostate Cancer Progression through Activating PI3K-AKT-mTOR Signaling. *Prostate* **2018**, *78*, 166−177.
(61) Xie, L.; Yi, J.; Song, Y.; Zhao, M.; Fan, L.; Zhao, L. Suppression of GOLM1 by EGCG through HGF/HGFR/AKT/GSK-3β/β-catenin/c-Myc Signaling Pathway Inhibits Cell Migration of MDA-MB-231. *Food Chem. Toxicol.* **2021**, *157*, 112574.
(62) Xu, W. N.; Zheng, H. L.; Yang, R. Z.; Jiang, L. S.; Jiang, S. D. HIF-1α Regulates Glucocorticoid-Induced Osteoporosis through PDK1/AKT/mTOR Signaling Pathway. *Front Endocrinol (Lausanne)* **2020**, *10*, 922.
(63) Zhang, J.; Liu, X.; Li, H.; Chen, C.; Hu, B.; Niu, X.; Li, Q.; Zhao, B.; Xie, Z.; Wang, Y. Exosomes/Tricalcium Phosphate Combination Scaffolds Can Enhance Bone Regeneration by Activating the PI3K/Akt Signaling Pathway. *Stem Cell Res. Ther.* **2016**, *7*, 136.
(64) Kladney, R. D.; Bulla, G. A.; Guo, L.; Mason, A. L.; Tollefson, A. E.; Simon, D. J.; Koutoubi, Z.; Fimmel, C. J. GP73, a Novel Golgi-Localized Protein Upregulated by Viral Infection. *Gene* **2000**, *249*, 53−65.
(65) Yan, J.; Zhou, B.; Li, H.; Guo, L.; Ye, Q. Recent Advances of GOLM1 in Hepatocellular Carcinoma. *Hepat. Oncol.* **2020**, *7*, Hep22.
(66) Wright, L. M.; Yong, S.; Picken, M. M.; Rockey, D.; Fimmel, C. J. Decreased Survival and Hepato-Renal Pathology in Mice with C-terminally Truncated GP73 (GOLPH2). *Int. J. Clin. Exp. Pathol.* **2009**, *2*, 34−47.
(67) Thon, J. N.; Italiano, J. E. Platelets: Production, Morphology and Ultrastructure. *Handb. Exp. Pharmacol.* **2012**, *210*, 3−22.
(68) Yap, T. A.; Yan, L.; Patnaik, A.; Fearen, I.; Olmos, D.; Papadopoulos, K.; Baird, R. D.; Delgado, L.; Taylor, A.; Lupinacci, L.; Riisnaes, R.; Pope, L. L.; Heaton, S. P.; Thomas, G.; Garrett, M. D.; Sullivan, D. M.; de Bono, J. S.; Tolcher, A. W. First-in-Man Clinical Trial of the Oral Pan-AKT Inhibitor MK-2206 in Patients with Advanced Solid Tumors. *J. Clin. Oncol.* **2011**, *29*, 4688−4695.
(69) Xing, Y.; Lin, N. U.; Maurer, M. A.; Chen, H.; Mahvash, A.; Sahin, A.; Akcakanat, A.; Li, Y.; Abramson, V.; Litton, J.; Chavez-MacGregor, M.; Valero, V.; Piha-Paul, S. A.; Hong, D.; Do, K. A.; Tarco, E.; Riall, D.; Eterovic, A. K.; Wulf, G. M.; Cantley, L. C.; et al. Phase II Trial of AKT Inhibitor MK-2206 in Patients with Advanced Breast Cancer Who Have Tumors with PIK3CA or AKT Mutations, and/or PTEN Loss/PTEN Mutation. *Breast Cancer Res.* **2019**, *21*, 78.
(70) Badran, Z.; Abdallah, M. N.; Torres, J.; Tamimi, F. Platelet Concentrates for Bone Regeneration: Current Evidence and Future Challenges. *Platelets* **2018**, *29*, 105−112.
(71) Stroncek, D. F.; Rebulla, P. Platelet Transfusions. *Lancet* **2007**, *370*, 427−438.
(72) Etulain, J. Platelets in Wound Healing and Regenerative Medicine. *Platelets* **2018**, *29*, 556−568.
(73) Alsousou, J.; Ali, A.; Willett, K.; Harrison, P. The Role of Platelet-Rich Plasma in Tissue Regeneration. *Platelets* **2013**, *24*, 173−182.
(74) Bachurski, D.; Schuldner, M.; Nguyen, P.-H.; Malz, A.; Reiners, K. S; Grenzi, P. C; Babatz, F.; Schauss, A. C; Hansen, H. P; Hallek, M.; von Strandmann, E. P. Extracellular Vesicle Measurements with Nanoparticle Tracking Analysis - an Accuracy and Repeatability Comparison between NanoSight NS300 and ZetaView. *J. Extracell. Vesicles* **2019**, *8*, 1596016.
(75) Rubak, P.; Kristensen, S. D.; Hvas, A. M. Flow Cytometric Analysis of Platelet Cyclooxygenase-1 and −2 and Surface Glycoproteins in Patients with Immune Thrombocytopenia and Healthy Individuals. *Platelets* **2017**, *28*, 387−393.
(76) Zlotogorski-Hurvitz, A.; Dayan, D.; Chaushu, G.; Korvala, J.; Salo, T.; Sormunen, R.; Vered, M. Human Saliva-Derived Exosomes: Comparing Methods of Isolation. *J. Histochem. Cytochem.* **2015**, *63*, 181−189.
(77) Chen, S.; Tang, Y.; Liu, Y.; Zhang, P.; Lv, L.; Zhang, X.; Jia, L.; Zhou, Y. Exosomes Derived from MiR-375-Overexpressing Human Adipose Mesenchymal Stem Cells Promote Bone Regeneration. *Cell Prolif.* **2019**, *52*, No. e12669.
(78) Zhu, Y.; Zhang, X.; Gu, R.; Liu, X.; Wang, S.; Xia, D.; Li, Z.; Lian, X.; Zhang, P.; Liu, Y.; Zhou, Y. LAMA2 Regulates the Fate Commitment of Mesenchymal Stem Cells via Hedgehog Signaling. *Stem Cell Res. Ther.* **2020**, *11*, 135.
(79) Liu, X.; Liu, X.; Du, Y.; Hu, M.; Tian, Y.; Li, Z.; Lv, L.; Zhang, X.; Liu, Y.; Zhou, Y.; Zhang, P. DUSP5 Promotes Osteogenic Differentiation through SCP1/2-Dependent Phosphorylation of SMAD1. *Stem Cells* **2021**, *39*, 1395−1409.
(80) Jin, C.; Zhang, P.; Zhang, M.; Zhang, X.; Lv, L.; Liu, H.; Liu, Y.; Zhou, Y. Inhibition of SLC7A11 by Sulfasalazine Enhances Osteogenic Differentiation of Mesenchymal Stem Cells by Modulating BMP2/4 Expression and Suppresses Bone Loss in Ovariectomized Mice. *J. Bone Miner Res.* **2017**, *32*, 508−521.
(81) Bouxsein, M. L.; Boyd, S. K.; Christiansen, B. A.; Guldberg, R. E.; Jepsen, K. J.; Müller, R. Guidelines for Assessment of Bone Microstructure in Rodents Using Micro-Computed Tomography. *J. Bone Miner Res.* **2010**, *25*, 1468−1486.

https://doi.org/10.1021/acsnano.3c07717
ACS Nano 2023, 17, 25070−25090